

Chemical evolution with radial mixing

Ralph Schönrich^{1*} and James Binney²

¹ *Universitätssternwarte München, Scheinerstr. 1, D-81679 München, D*

² *Rudolf Peierls Centre for Theoretical Physics, Keble Road, Oxford OX1 3NP, UK*

Draft, September 4, 2008

ABSTRACT

Models of the chemical evolution of our Galaxy are extended to include radial migration of stars and flow of gas through the disc. The models track the production of both iron and α elements. A model is chosen that provides an excellent fit to the metallicity distribution of stars in the Geneva–Copenhagen survey (GCS) of the solar neighbourhood, and an acceptable fit to the local Hess diagram. The model provides a good fit to the distribution of GCS stars in the age–metallicity plane although this plane was not used in the fitting process. Although this model’s star-formation rate is monotonic declining, its disc naturally splits into an α -enhanced thick disc and a normal thin disc. In particular the model’s distribution of stars in the $([\text{O}/\text{Fe}], [\text{Fe}/\text{H}])$ plane resembles that of Galactic stars in displaying a ridge line for each disc. The thin-disc’s ridge line is entirely due to stellar migration and there is the characteristic variation of stellar angular momentum along it that has been noted by Haywood in survey data. Radial mixing of stellar populations with high σ_z from inner regions of the disc to the solar neighbourhood provides a natural explanation of why measurements yield a steeper increase of σ_z with age than predicted by theory. The metallicity gradient in the ISM is predicted to be steeper than in earlier models, but appears to be in good agreement with data for both our Galaxy and external galaxies. The absolute magnitude of the disc is given as a function of time in several photometric bands, and radial colour profiles are plotted for representative times.

Key words: galaxies: abundances - galaxies: evolution - galaxies: ISM - galaxies: kinematics and dynamics - Galaxy: disc - solar neighbourhood

1 INTRODUCTION

Models of the chemical evolution of galaxies are key tools in the push to understand how galaxies formed and have evolved. Their application to our Galaxy is of particular importance both on account of the wealth of observational data that they can be required to reproduce, and on account of the inherent interest in deciphering the history of our environment.

From the pioneering papers by van den Bergh (1962) and Schmidt (1963) it has generally been assumed that a galaxy such as the Milky Way can be divided into concentric cylindrical annuli, each of which evolves independently of the others – see for example Pagel (1997). The contents of any given cylinder are initially gaseous and of extremely low or zero metallicity. Over time stars form in the cylinder and the more massive ones die, returning a mixture of heavy elements to the remaining gas. The consequent increase in the metallicity of the gas and newly-formed stars is generally

moderated by an inflow of gas from intergalactic space, and, less often, by an outflow of supernova-heated gas.

The cool, star-forming gas within any cylinder is assumed to be well mixed, so at any time it can be characterised by a metallicity $Z(r, t)$, where r is the cylinder’s radius. Hence the stars formed within a given cylinder should have metallicities $Z(r, t_f)$ that are uniquely related to their time of formation, t_f . Observations do not substantiate this prediction; in fact Edvardsson et al. (1993) showed that solar-neighbourhood stars are widely distributed in the (t_f, Z) plane – for a detailed discussion see Haywood (2006).

The absence of an age–metallicity relation in the solar neighbourhood is naturally explained by radial migration of stars (Sellwood & Binney 2002; Haywood 2008). It has been recognised for many years that scattering by spiral structure and molecular clouds gradually heats the stellar disc, moving stars onto ever more eccentric and inclined orbits. Stars that are on eccentric orbits clearly contribute to different cylindrical annuli at different phases of their orbits, and thus tend to blur any radial gradient in the metallicities of newly formed stars. Moreover, scattering events also change

* E-mail: rasch@usm.lmu.de

the guiding centres of stellar orbits, so even a star on a circular orbit can be found at a different radius from that of its birth. In fact, Sellwood & Binney (2002) argued that the dominant effect of transient spiral structure is resonant scattering of stars across the structure’s corotation resonance, so even a star that is still on a near-circular orbit may be far from its radius of birth. Roskar et al. (2008) showed that in a cosmological simulation of galaxy formation that included both stars and gas, resonant scattering at corotation caused stars to move outwards and gas inwards, with the result that the stellar disc extended beyond the outer limit of star formation; the outer disc was entirely populated by stars that had formed much further in and yet were still on nearly circular orbits. This simulation confirmed the conjecture of Sellwood & Binney (2002) that gas would participate in resonant scattering alongside stars.

We distinguish two drivers of radial migration: when the angular momentum of a star is changed, whether by scattering at an orbital resonance or by non-resonant scattering by a molecular cloud, the star’s guiding-centre radius changes and the star’s entire orbit moves inwards or outwards depending on whether angular momentum is lost or gained. When a scattering event increases a star’s epicycle amplitude without changing its angular momentum, the star contributes to the density over a wider range of radii. In a slight modification of the terminology introduced by Sellwood & Binney (2002), we say that changes in angular momentum are caused by “churning” while changes in epicycle amplitude lead to “blurring”. This paper extends models of Galactic chemical evolution to include the effects of churning and blurring.

Given the strength of the arguments that gas should participate in churning alongside stars, and that shocks induced by spiral structure cause gas to drift inwards, it is mandatory simultaneously to extend traditional chemical evolution models to include radial flows of gas within the disc, and we do this.

The paper is organized as follows. Section 2 presents the equations upon which the models are based. These consist of the rules that determine the rate of infall of fresh gas, the rate of star formation, details of the stellar evolution tracks and chemical yields that we have used and descriptions of how churning and blurring are implemented. Section 3 describes in some detail a “standard” model of the evolution of the Galactic disc. This covers its global properties but focuses on what would be seen in a survey of the solar neighbourhood. Section 4 presents the rather intricate details of the selection function that is required to mimic the Geneva–Copenhagen sample (GCS) of solar-neighbourhood stars published by Nordström et al. (2004), and explains how this sample has been used to constrain the model’s parameters. Section 5 explains how the observable properties of the model depend on its parameters. Section 6 discusses the relation of the present models to earlier ones, and discusses the extent to which it is consistent with the analysis of solar-neighbourhood data by Haywood (2008). Section 7 sums up.

2 GOVERNING EQUATIONS

The simulation is advanced by a series of discrete timesteps of duration 30 Myr.

The disc is divided into 80 annuli of width 0.25 kpc and central radii that range from 0.125 kpc to 19.875 kpc. In each annulus there is both cold (~ 30 K) and warm ($\gtrsim 10^4$ K) gas with specified abundances (Y, Z) of helium and heavy elements. Within the latter we keep track of the abundances of O, C, Mg, Si, Ca and Fe. Each annulus has a stellar population for each elapsed timestep, and this population inherits the abundances Y, Z , etc., of the local cold gas. At each stellar mass, the stellar lifetime is determined by the initial abundances, and at each age we know the luminosity and colours of such of its stars that are not yet dead. Each stellar population is at all times associated with the annulus of its birth; the migration of stars is taken into account as described below only when returning matter to the ISM or constructing an observational sample of stars.

The whole field of chemical modelling has been thrown into turmoil by the discovery that three-dimensional, non-equilibrium models of the solar atmosphere require the metal abundance of the Sun to be $Z_{\odot} = 0.012 - 0.014$ (Grevesse et al. 2007) rather than the traditional value ~ 0.019 . This work suggests that the entire metallicity scale needs to be thoroughly reviewed: if the Sun’s metallicity has to be revised downwards, then so will the metallicities of most nearby stars. Crucially there is the possibility that values for the metallicity of the ISM require revision: some values derive from measurements of the metallicities of short-lived stars such as B stars and require downward revision (e.g. Daflon & Cunha 2004), while others are inferred from measurements of the strengths of interstellar emission lines, and are not evidently affected by changes in stellar metallicities. If the metallicity scale of stars were lowered while that of the ISM remained substantially unaltered, it would be exceedingly hard to construct a viable model of the chemical evolution of the solar neighbourhood. Moreover, both the stellar catalogue and most of the measurements of interstellar abundances with which we wish to compare our models are on the old metallicity scale, and unphysical anomalies will become rife as soon as one mixes values on the old scale with ones on the new. Therefore for consistency we use the old solar abundance $Z_{\odot} = 0.019$ and exclude from considerable metallicity values that are on the new scale.

2.1 Star-formation law

Stars form according to the Kennicutt (1998) law. Specifically, with the surface density of cold gas Σ_g measured in $M_{\odot} \text{ pc}^{-2}$ and t in Myr, star formation increases the stellar surface density at a rate

$$\frac{d\Sigma_*}{dt} = 1.2 \times 10^{-4} \begin{cases} \Sigma_g^{1.4} & \text{for } \Sigma_g > \Sigma_{\text{crit}} \\ C\Sigma_g^4 & \text{otherwise,} \end{cases} \quad (1)$$

where the threshold for star formation, Σ_{crit} is a parameter of the model and $C = \Sigma_{\text{crit}}^{-2.6}$ ensures that the star-formation rate is a continuous function of surface density.

The stars are assumed to be distributed in initial mass over the range $(0.1, 100) M_{\odot}$ according to the Salpeter function, $dN/dM \propto M^{-2.35}$. The luminosities, effective temperatures, colours and lifetimes of these stars are taken by linear

interpolation in (Y, Z) from the values given in the BASTI database (Cassisi et al. 2006).

2.2 Return of metals

The nucleosynthetic yields of individual metals are in many cases still subject to significant uncertainties (e.g. Thomas et al. 1998); in fact models of the chemical evolution of the solar neighbourhood have been used to constrain these yields (Francois et al. 2004).

For initial masses in the ranges $5 - 11 M_{\odot}$ and $35 - 100 M_{\odot}$ values of X, Y, Z, C and O were taken from Maeder (1992) using a non-linear interpolation scheme: the paper gives yields for $Z = 10^{-4}$ (Y_{LZ} denotes the yields for low metallicity models) and $Z = 0.02$ (Y_{HZ}) and guided by the metallicity-dependence of the sizes of CO cores reported by Portinari et al. (1998) we take

$$Y(Z) = (1 - \alpha)Y_{LZ} + \alpha Y_{HZ}, \quad (2)$$

where

$$\alpha = \begin{cases} 0 & \text{for } Z < 0.005 \\ 640(Z - 0.005) & \text{for } 0.005 < Z < 0.0075 \\ 0.8 + 16(Z - 0.0075) & \text{for } 0.0075 < Z < 0.02 \\ 1 & \text{for } Z > 0.02 \end{cases} \quad (3)$$

The yields of elements other than X, Y, Z, C and O from stars with masses in this range were taken from the *ORFEO* database of Limongi & Chieffi (2008) with the mass cut set such that $0.05 M_{\odot}$ of ^{56}Ni is produced; this relatively low mass cut reproduces the Ca/Fe ratio measured in very metal-poor stars by Lai et al. (2008). Stars less massive than $10 M_{\odot}$ were assumed to produce no elements heavier than O . For stars with masses $< 5 M_{\odot}$, the yields were taken in a linear interpolation from Marigo (2001).

For initial stellar masses in the range $11 - 35 M_{\odot}$ we used the metallicity-dependent yields of heavy elements from Chieffi & Limongi (2004) in a linear interpolation on mass and metallicity, extrapolating up to $\alpha = 1.5$ or $Z = 0.03$ respectively.

A fraction f_{eject} of the gas ejected by dying stars leaves the Galaxy; we tested models with $0 \leq f_{\text{eject}} \leq 0.05$ (Pagel 1997). Increasing f_{eject} has the effect of reducing the final metallicity of the disc; in fact there is almost complete degeneracy between the values of f_{eject} and nucleosynthetic yields. In view of the evidence that star formation near the Galactic centre drives a Galactic wind (Bland-Hawthorn & Cohen 2003), we set $f_{\text{eject}} = 0.15$ at $R < 3.5 \text{ kpc}$ in models that use the accretion law (6) below. At all other radii we set $f_{\text{eject}} = 0.04$.

A fraction f_{direct} of the ejecta goes straight to the cold gas reservoir of the local annulus, and the balance goes to the annulus's warm-gas reservoir. Setting f_{direct} to values ~ 0.2 has a significant impact on the number of extremely metal-poor stars predicted near the Sun. However, such large values of f_{direct} are not well motivated physically, and in the models presented here $f_{\text{direct}} = 0.01$ has a negligible value.

In each timestep δt a fraction $\delta t/t_{\text{cool}}$ of the warm gas cools and enters the cold-gas reservoir. The parameter t_{cool} is determined by the balance between radiative cooling and shock heating of the warm gas. Consequently, its value cannot be determined a priori from atomic physics. Increasing t_{cool} increases the mass of gas in the warm reservoir, and re-

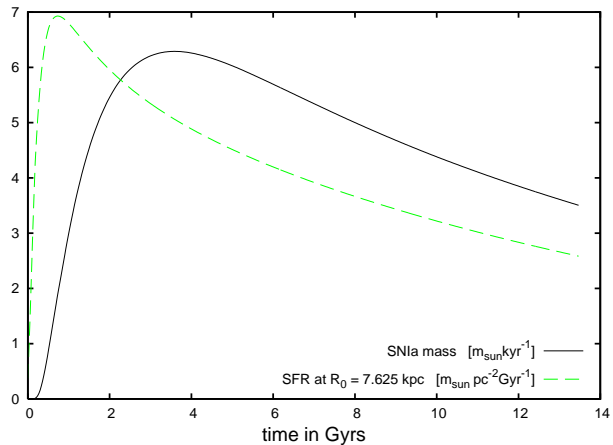


Figure 1. The rate of mass injection by SNIa in the standard model (solid black line). The broken green line gives the star formation rate in the solar annulus.

duces the SFR. It is thought that in excess of 10 percent of the Galaxy's gas is in the warm phase. In fact the warm-gas reservoir should include extraplanar HI as well as genuinely hot gas, because it should encompass all gas that is unavailable for star formation. In NGC 891 of order a third of the galaxy's HI is extraplanar (Oosterloo et al. 2007), so the warm-gas reservoir is potentially massive. We have worked with values $t_{\text{cool}} \gtrsim 1 \text{ Gyr}$ that yield warm-gas fractions of order 10 percent. Increasing t_{cool} also increases the number of very metal-poor stars formed, and lengthens the period in which star formation is α -enhanced.

Initially there is $5 \times 10^8 M_{\odot}$ of warm gas and the rest is cold. The warm gas is assumed to be pre-enriched by the halo. For the chemical composition we use the state of the warm ISM after two timesteps. $1.25 \times 10^8 M_{\odot}$ of gas is added to the disc at each of the next four timesteps. The surface density of the added gas was proportional to

$$(1.0 - e^{(R-19.8 \text{ kpc})/11.8 \text{ kpc}})e^{-R/4 \text{ kpc}}. \quad (4)$$

Thus the surface density was exponential with scalelength 4 kpc inside $\sim R_0$ but tapered to zero at the outer edge of the grid. The existence at the outset of a warm, pre-enriched component of the ISM is physically well motivated and proves the most effective way of producing the right number of metal-poor stars.

Type Ia supernovae were included by assuming that 7.5 per cent of the mass in white dwarfs formed by stars of initial mass 3.2 to $8.5 M_{\odot}$ ultimately explodes in type Ia supernovae. The yields were taken to be those of the W70 model in Iwamoto et al. (1999). It is believed that the progenitors of type Ia supernovae have lifetimes of order a Gyr (Förster et al. 2006) and we have taken the mass M_{WD} of the population that survives to time t from white-dwarf formation to satisfy

$$\frac{dM_{\text{WD}}}{dt} = \begin{cases} 0 & \text{for } t < 0.15 \text{ Gyr} \\ -M_{\text{WD}}/1.5 \text{ Gyr} & \text{otherwise.} \end{cases} \quad (5)$$

The rate of type Ia SNe is constrained by the requirements that $[\text{O/Fe}]$ has to fall from ~ 0.6 for the oldest stars to around -0.1 , and that $[\text{Ca/Fe}]$ should go from about ~ 0.3 to ~ 0 . Fig. 1 shows the resulting mass-return rate in the best-fitting model.

2.3 Inflow

It is generally agreed that viable models of galactic chemical evolution require the disc to be constantly fed with gas from intergalactic space; inflow resolves several serious problems, including (i) the appearance of too many low-metallicity stars near the Sun (the “G-dwarf problem”, e.g. Pagel 1997), (ii) excessive metallicity of the current ISM, (iii) an unrealistically low abundance of deuterium in the current ISM. Moreover, both the short timescale for the current ISM to be consumed by star formation and direct manifestations of infalling gas (Sancisi et al. 2008) argue strongly for the existence of inflow. Unfortunately, many aspects of inflow are extremely uncertain. We find that the predictions of our models depend sensitively on how these uncertainties are resolved, so to the extent that other aspects of our models have sound foundations, they can usefully constrain the nature of inflow.

2.3.1 Infall rate

We have investigated two approaches to the determination of the inflow rate. The first starts with a quantity of gas ($8 \times 10^9 M_\odot$) and feeds gas into it at a rate

$$\dot{M} = \frac{M_1}{b_1} e^{-t/b_1} + \frac{M_2}{b_2} e^{-t/b_2}. \quad (6)$$

Here $b_1 \simeq 0.2$ Gyr is a short timescale that ensures that the star-formation rate peaks early on, while $b_2 \simeq 14$ Gyr is a long timescale associated with sustained star formation in the thin disc. We adopt $M_1 \simeq 9.7 \times 10^9 M_\odot$ and choose M_2 such that after 12 Gyr the second exponential has delivered $2.6 \times 10^{10} M_\odot$.

In an alternative scheme, the gas mass within the disc is determined a priori and inflow is assumed to be available to maintain the gas mass at its prescribed level. We have investigated schemes in which the gas mass declines exponentially with time, but focused on models in which it is held constant at $8.4 \times 10^9 M_\odot$; models in which the gas mass declines exponentially produce very similar results to models in which the inflow declines exponentially.

2.3.2 Distribution of inflow

It proves extremely hard to devise a satisfactory algorithm for determining the radial distribution of infalling gas. We have experimented with two schemes and found that acceptable models can only be obtained by using a combination of them.

Underlying both schemes is the principle that the surface-density of gas is at all times exponential, $\Sigma_g(R) \propto e^{-R/R_d}$, where $R_d = 3.5$ kpc is chosen such that with the star-formation law adopted above, the inner stellar disc acquires a scale length $R_* = R_d/1.4 = 2.5$ kpc similar to that determined from star counts (Robin et al. 2003; Juric et al. 2008). Given the exponential surface density, the mass of gas in each ring is a fixed fraction of the total gas mass.

Either of the algorithms of the last subsection specifies what the total gas mass should be at the start of a timestep: this is either the prescribed constant or, when equation (6) is used, it is the mass in the disc at the end of the previous timestep plus the amount that falls in during the most recent

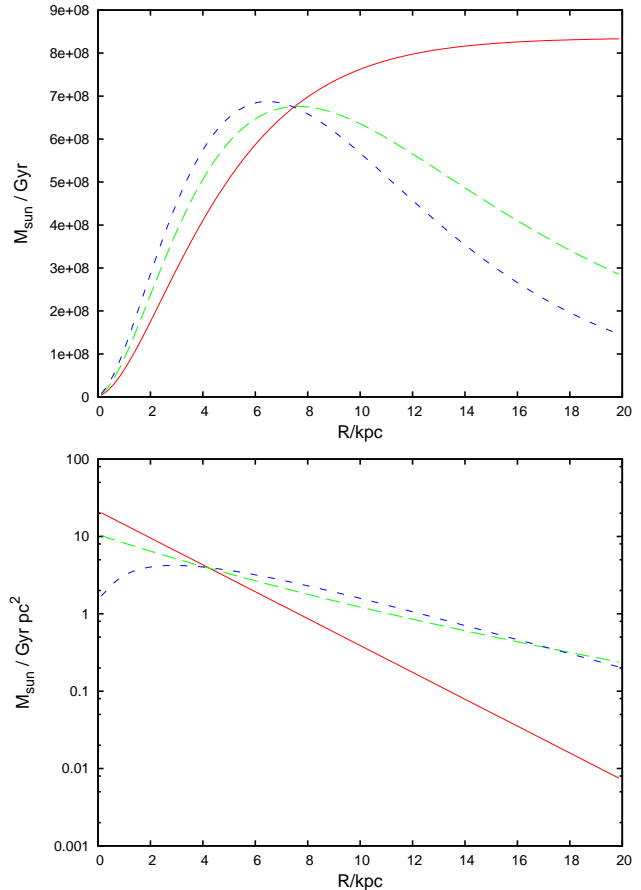


Figure 2. Upper panel: examples of flows through the disc induced by inflow Scheme A with $f_A = 0.5$ (red curve), inflow Scheme B with $f_B = 0.042$ (blue short dashed curve), and inflow Scheme AB with $f_A = 0.23$ and $f_B = 0.025$ (green long dashed curve; the standard model). The quantity plotted is the rate of flow of gas over the circle of radius R . Lower panel: the corresponding rates of accretion from the IGM per unit area of the disc.

timestep. Hence the mass that should be in each annulus at the start of a timestep follows from the assumed exponential profile of the gas disc. Subtracting from this the mass that was present after the previous timestep, we calculate the need, i.e. the amount of gas that has to be added, of the i th annulus ΔM_i .

Both inflow schemes fill annuli up with gas in sequence, starting with the innermost ring 0. In Scheme A this annulus receives $f_A \Delta M_0$ from the IGM, and grabs the balance, $(1 - f_A) \Delta M_0$, from annulus 1, where $f_A \simeq 0.2$ is a parameter of the model. Annulus 1 receives $f_A \Delta M_1$ from the IGM, and grabs the balance of its requirement, $(1 - f_A)(\Delta M_1 + \Delta M_0)$, from annulus 2. The updating of every annulus proceeds similarly, until the last annulus is reached, which covers its entire need from the IGM. The characteristic of Scheme A is the development of a large flux of gas through the outer rings – an example is given by the red curve in the upper panel of Fig. 2. This flux transports inwards metals synthesised in these rings and tends to deposit them at intermediate radii, where the inward flux is diminishing.

In Scheme B annulus 0 obtains $f_B \Delta M_0$ from the IGM and the rest from annulus 1. Annulus 1 now obtains

$f_B[\Delta M_1 + (1 - f_B)\Delta M_0]$ from the IGM, and so on to the outermost ring, which is again entirely fed by the IGM.

In both schemes a fixed fraction of each annulus's need is taken from the IGM, but the definition of “need” is different in the two schemes: in Scheme B it includes the gas that was taken from it by its inner neighbour, and in Scheme A it does not. In Scheme B the amount taken from the IGM builds up from the centre outwards, so a smaller fraction of the infalling gas goes directly to the centre. Since more of the gas entering the centre has flowed through the disc, the central metallicity rises more rapidly than in Scheme A. The short dashed blue curve in the upper panel of Fig. 2 shows a typical example of a mass flow through the disc with Scheme B. Whereas the flow generated by Scheme A (red curve) increases monotonically from the centre, the Scheme-B flow rises quickly with galactocentric distance R near the centre but then peaks at $R \simeq 5$ kpc. In the outer region in which the inflow is small, the metallicity forms a plateau. The extent of this plateau is controlled by f_B : the larger f_B , the smaller the radius at which the inflow rate peaks and the further in the metallicity plateau extends.

Scheme A enhances the metallicity of the middle section of the disc and causes the metallicity gradient to be steepest towards the outside of the disc, Scheme B enhances the metallicity of the inner disc and flattens the gradient at large radii.

In Scheme A, if f_A is set too low, the flux of gas through the outer annuli becomes implausibly large in relation to the mass of gas that is in these annuli, and radial flow velocities $v_R \gtrsim 20 \text{ km s}^{-1}$ are predicted. In Scheme B f_B can be quite small because, although the flow of gas through the disc builds up more quickly at small radii, it peaks at a few kiloparsecs and then declines to small values in the outer disc. If either f_A or f_B is large, the flow through the disc becomes small and the metallicity of the solar neighbourhood becomes unrealistically large through the accumulation of metals created at the solar radius and beyond.

We were able to obtain satisfactory fits to the data only by combining Schemes A and B. In the Scheme AB annulus 0 receives a mass $(f_A + f_B)\Delta M_0$ from the IGM and grabs the balance $M_{01} = (1 - f_A - f_B)\Delta M_0$ from annulus 1. Annulus 1 receives a mass $f_A\Delta M_1 + f_B(\Delta M_1 + M_{01})$ from the IGM and grabs the balance of its requirement from annulus 2, and so on. Notice that the radial flow profile in Scheme AB is not simply the sum of the corresponding profiles for Schemes A and B used alone. The green curve in the upper panel of Fig. 2 shows the radial flow profile obtained with Scheme AB.

For each accretion scheme, the lower panel of Fig. 2 shows the corresponding radial distribution of accretion from the IGM.

2.3.3 Metallicity of the IGM

We have to prescribe the metallicity and alpha-enhancement of gas taken from the IGM. It is far from clear how this should be done.

There is abundant evidence that pristine intergalactic gas disappeared from the IGM long ago: quasar absorption line-studies reveal an early build up of heavy elements in the IGM (Pettini et al. 2003). Moreover, the handful of high-velocity clouds for which metallicities have been mea-

sured, have heavy-element abundances of order a tenth solar (Wakker 2000). Finally, the metallicities of the most metal-poor thick-disc stars are similar to the metallicities of the most metal-rich halo stars, which suggests that the early disc was pre-enriched by the halo. We assume that throughout the simulation accreted gas has metallicity $Z = 0.1Z_\odot$.

Given that the thick disc is alpha-enhanced (Venn et al. 2004), it is clear that when disc formation starts, infalling gas must be alpha-enhanced. It is natural that this enhancement should decline with time as Fe from type Ia SNe finds its way into the IGM. Indeed, in addition to gas ejected from the Galaxy, type Ia SNe in dwarf spheroidal galaxies will have contributed their Fe to the local IGM, and if the Magellanic Stream is made of gas torn from the SMC, it will have been enriched with Fe from SNe in the SMC. Thus we expect the metallicity and alpha enhancement of the IGM to be time dependent and governed by the chemical-evolution histories of galaxies.

These considerations suggest making the abundances of the IGM reflect those of an outer annulus of the Galaxy; the chemical evolution of this ring acts as a proxy for the combined chemical evolution of the many contributors to the chemical evolution of the IGM. If the IGM were assumed to mirror the outermost ring, its metallicity would remain extremely low because this annulus takes all its gas from the IGM, and passes what few heavy elements it synthesises inwards. Hence the IGM must mirror an outer annulus but not the outermost. In our models the IGM mirrors the annulus with radius $R = 12.125$ kpc. Since yields of α elements decline with increasing metallicity, the outer disc should be α -enhanced.

2.4 Churning

Transient spiral arms cause both stars and gas to be exchanged between annuli in the vicinity of the corotation resonance. The process conserves angular momentum. We take the process to be made up of a large number of exchanges between adjacent rings; in each timestep there are two such exchanges, so within a timestep second-nearest neighbouring rings exchange mass. The probability p_{ij} that in a given half-timestep a star or gas cloud in the i th annulus is transferred to the j th annulus is

$$p_{ij} = \begin{cases} k_{\text{ch}} M_j / M_{\text{max}} & \text{for } j = i \pm 1 \\ 0 & \text{otherwise,} \end{cases} \quad (7)$$

where M_j is the mass of gas and stars in the j th annulus and $M_{\text{max}} = \max_j(M_j)$. This rule ensures that the mass transferring outwards from the i th annulus is proportional to $M_i M_{i+1}$, and an equal mass transfers inwards. This condition would still hold if we divided the right-hand side of equation (7) by any power of $M_i + M_j$. However, we want the churning rate to reflect the local gravitational instability of the disc, so a rate that scales quadratically with ring mass seems appropriate. The constant k_{ch} is thus the largest transition probability for any annulus. It is treated as a free parameter to be fitted to the data. The procedure for distributing the metals released by a population of stars born in annulus i is as follows. The probability that a star born in annulus i at timestep m is found to be in annulus j at timestep n is equal to the ij th element of the product matrix $\mathbf{p}_m \mathbf{p}_{m+1} \times \dots \times \mathbf{p}_n$. In practice we recompute \mathbf{p} only each

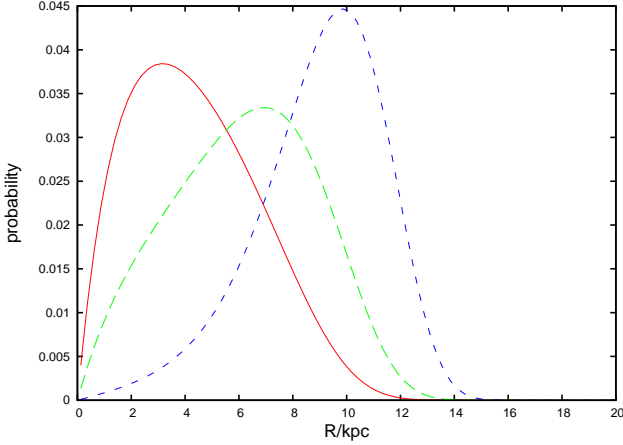


Figure 3. The radial distribution of the guiding centres of 12 Gyr-old stars that were born at 5 (red), 7.6 (green, long dashed) and 10 kpc (blue, short dashed) when the churning fraction $k_{\text{ch}} = 0.35$.

five timesteps and approximate $\mathbf{p}_m \times \cdots \mathbf{p}_{m+4}$ by \mathbf{p}_m^5 . Fig. 3 shows the extent to which the guiding centres of stars are changed over the lifetime of the Galaxy when $k_{\text{ch}} = 0.35$.

2.5 Blurring

In addition to changing their guiding-centre radii through the churning process, stars oscillate around their guiding centres with steadily increasing amplitudes. Consequently, stars spend time away from their guiding-centre radii. For simplicity, we assume in this section that the circular speed v_c is independent of radius and that the vertical motion can be ignored because it decouples from motion in the plane.

The fraction of its time that the orbit with energy and angular momentum E, L spends in a radial interval $(R, R + dR)$ is

$$dp = \frac{dt}{T} = \frac{1}{T} \frac{dR}{v_R} = \frac{\Omega_R}{\pi} \frac{dR}{\sqrt{2(E - \Phi_{\text{eff}})}}, \quad (8)$$

where $T \equiv \pi/\Omega_R$ is the half period and $\Phi_{\text{eff}}(R, L) \equiv \Phi(R) + L^2/2R^2$ is the effective potential. We need to average this over all stars with given L . These stars have some distribution over the energy $E = \frac{1}{2}v_R^2 + \Phi_{\text{eff}}$. It is expedient to decompose E into the energy $\Phi_c(L) \equiv \Phi(R_c) + L^2/2R_c^2$ of the circular orbit (with radius R_c) of angular momentum L and the random energy $\mathcal{E} \equiv E - \Phi_c$. Following Shu (1969) we take the distribution function (DF) to be

$$f(\mathcal{E}, L) = \frac{F(L)}{\sigma^2} e^{-\mathcal{E}/\sigma^2}, \quad (9)$$

which ensures that the radial velocity dispersion is approximately (but not exactly) σ . Normalizing f such that $\int dL dJ_R f = 1$, where $J_R(\mathcal{E})$ is the radial action, the probability that a randomly chosen star lies in $(R, R + dR)$ is $\int dL dJ_R f dp$. Recalling that $dL dJ_R = dL d\mathcal{E}/\Omega_R$ and substituting for f and dp , we find that the number of stars in the annulus is

$$dn(R) = \int dL dJ_R (f dp)$$

$$\begin{aligned} &= \frac{NdR}{\pi} \int dL \frac{F}{\sigma^2} \int_{\Phi_{\text{eff}} - \Phi_c}^{\infty} d\mathcal{E} \frac{e^{-\mathcal{E}/\sigma^2}}{\sqrt{2(\mathcal{E} + \Phi_c - \Phi_{\text{eff}})}} \quad (10) \\ &= \frac{NdR}{\sqrt{2}\pi} \int dL \frac{F}{\sigma^2} e^{[\Phi_c - \Phi_{\text{eff}}]/\sigma^2} \int_0^{\infty} dx \frac{e^{-x/\sigma^2}}{\sqrt{x}}, \end{aligned}$$

where N is the total number of stars in the system. The integral over x is simply $\sigma \int dt e^{-t}/\sqrt{t} = \sqrt{\pi}\sigma$. Thus we can conclude that the probability per unit area associated with a star of given L is

$$P(R) = \frac{dn}{N2\pi R dR} = \frac{K}{\sigma R} \exp\left[\frac{\Phi_c(L) - \Phi_{\text{eff}}(R, L)}{\sigma^2}\right], \quad (11)$$

where K is chosen such that $1 = 2\pi \int dR R P(R)$.

The parameter σ used in these formulae is actually smaller than the rms radial velocity dispersion, which is given by

$$\langle v_R^2 \rangle = \frac{\sqrt{2\pi}}{R\Sigma} \int dL F \sigma \exp[(\Phi_c - \Phi_{\text{eff}})/\sigma^2], \quad (12)$$

where the stellar surface density is

$$\Sigma(R) = \frac{\sqrt{2\pi}}{R} \int dL \frac{F}{\sigma} \exp[(\Phi_c - \Phi_{\text{eff}})/\sigma^2]. \quad (13)$$

For specified radial dependencies of Σ and $\langle v_R^2 \rangle$, equations (12) and (13) can be used to determine the functions $F(L)$ and $\sigma(L)$ (Dehnen 1999). However, in the present application it is not $\Sigma(R)$ that we wish to specify, but the number of stars with guiding centres in each ring:

$$\begin{aligned} \frac{dN}{dR_c} &= v_c N_{\text{tot}} \frac{dN}{dL} = v_c \int dJ_R f(L, J_R) \\ &= \frac{v_c F N_{\text{tot}}}{\sigma^2} \int \frac{d\mathcal{E}}{\Omega_R} e^{-\mathcal{E}/\sigma^2}, \end{aligned} \quad (14)$$

where N_{tot} is the total number of stars in the disc. We adapt the technique described by Dehnen (1999) for determining $F(L)$ and $\sigma(L)$ from equations (12) and (13) to the determination of these quantities from equations (12) and (14). Specifically, we start from the values of $F(L)$ and $\sigma(L)$ that would hold in the epicycle approximation, when $\Omega_R = \kappa$ independent of \mathcal{E} and

$$F(L) = \frac{\kappa}{v_c N_{\text{tot}}} \frac{dN}{dR_c}. \quad (15)$$

Then at each L we evaluate $\langle v_R^2 \rangle$ from (12) and multiply σ by the ratio of the desired value to the value just calculated. Then we re-evaluate F from (14) and repeat until convergence is obtained.

We now address the question of how $\langle v_R^2 \rangle$ should depend on radius. The scale heights h of galactic discs are found to be largely independent of radius (van der Kruit & Searle 1982), and for $h \ll R$ (when the vertical dynamics can be considered one-dimensional) this finding implies that the vertical velocity dispersion scales with the surface density as $\Sigma^{1/2}$. If the ratio of the vertical and radial velocity dispersions $\sigma_z/\langle v_R^2 \rangle^{1/2}$ is independent of radius, as is often assumed (e.g. Kregel & van der Kruit 2005), then $\langle v_R^2 \rangle \propto \Sigma \propto e^{-R/R_*}$. In the solar neighbourhood at $R \simeq 3R_*$ the oldest stars have $\sigma_R \gtrsim 40 \text{ km s}^{-1}$, so this line of reasoning predicts that $\langle v_R^2 \rangle^{1/2} \gtrsim 180 \text{ km s}^{-1}$ at $R = R_*$, which is implausibly large.

Evidently these naive arguments based on complete

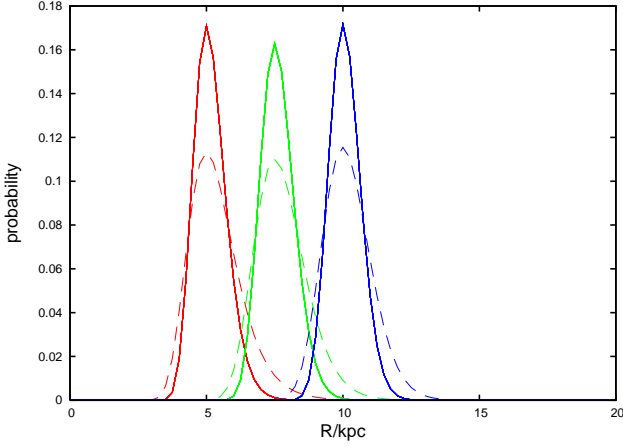


Figure 4. The radial distributions of stars with guiding centres at 5 (red), 7.6 (green) and 10 kpc (blue) when at the Sun $\langle v_R^2 \rangle^{1/2} = 25 \text{ km s}^{-1}$ (full curves) and 40 km s^{-1} (dashed curves).

decoupling of planar and vertical motions are inadequate for the old disc; we need a distribution function that treats the third integral properly. Pending the availability of such a DF we have adopted the assumption that $\langle v_R^2 \rangle \propto e^{-R/2R_*}$, which implies that at R_* the old disc has $\langle v_R^2 \rangle^{1/2} \simeq 85 \text{ km s}^{-1}$, which is only slightly lower than the velocity dispersion in the Galactic bulge (Rich et al. 2007).

From Binney et al. (2000) we take the time dependence of $\sqrt{\langle v_R^2 \rangle}(R_0)$ at solar galactocentric distance R_0 to be

$$\sqrt{\langle v_R^2 \rangle}(R_0, t) = \max \left\{ 10, 38 \left(\frac{t + 0.038 \text{ Gyr}}{10.038 \text{ Gyr}} \right)^{0.33} \right\} \text{ km s}^{-1}, \quad (16)$$

which is consistent with the data of Holmberg et al. (2007).

Fig. 4 shows blurring distributions $P(R)$ from equation (11) for three radii (5, 7.6 and 10 kpc) and two values of $\langle v_R^2 \rangle^{1/2}$ at the Sun, namely 25 km s^{-1} and 40 km s^{-1} .

Note that scatterings by spiral arms and molecular clouds that heat the disc, also change the angular momentum of each star and therefore its guiding centre. Hence such scatterings contribute to both churning and blurring.

Since churning moves the guiding centres of the stars themselves we first apply the churning matrix and apply the blurring matrix afterwards.

2.6 Vertical structure

For comparison with observations of the solar neighbourhood we need to know the vertical distribution of stars near the Sun. We determine this by adopting a relationship between time and vertical velocity dispersion (Binney et al. 2000)

$$\sigma_z(\tau) = \max \left\{ 4, 23 \left(\frac{\tau}{10 \text{ Gyr}} \right)^{0.33} \right\} \text{ km s}^{-1}. \quad (17)$$

Further assuming that stars of a given age form an isothermal population, their vertical density profile is

$$n(z) \propto e^{-\Phi(z)/\sigma_z^2}, \quad (18)$$

where $\Phi(z)$ is the difference in the gravitational potential between height z and the plane. This potential is calculated

Parameter	meaning	value
Σ_{crit}	Kennicutt's threshold surface density	0
M_0	initial gas mass	$1.5 \times 10^9 M_\odot$
M_1	early infall mass	$9.7 \times 10^9 M_\odot$
M_2	long timescale infall mass until 12 Gyrs	$2.6 \times 10^{10} M_\odot$
b_1	early infall timescale	0.21 Gyr
b_2	long infall timescale	14 Gyr
f_A	Scheme A fraction of gas from IGM	0.23
f_B	Scheme B fraction of gas from IGM	0.025
k_{ch}	churning amplitude	0.35
t_0	delay before first type Ia SNe	0.15 Gyr
k^{-1}	timescale for decay of type Ia SNe	1.5 Gyr
f_{eject}	fraction of ejecta lost to Galaxy	0.15 – 0.04
f_{direct}	fraction of ejecta to cold ISM	0.01
t_{cool}	cooling time of warm gas	1.2 Gyr
M_{warm}	initial warm gas mass	$5 \times 10^8 M_\odot$
Z_{IGM}	metallicity of the IGM	$0.1 Z_\odot$

Table 1. Parameters of the standard model. The infall rate is given by equation (6). The larger value of f_{eject} applies at $R < 3.5 \text{ kpc}$.

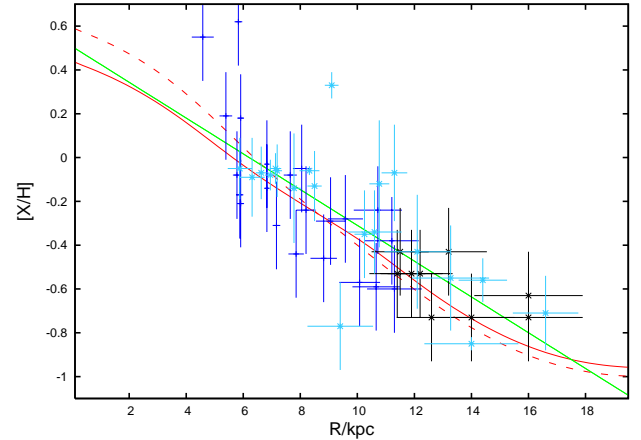


Figure 5. The metallicities of the current ISM in the standard model, $[Z/H]$ (red dashed curve) and $[O/H]$ (red full curve), as functions of Galactocentric radius. Also measurements of the metallicities of HII regions by Shaver et al. (1983) (dark blue), Vilchez & Esteban (1996) (black crosses) and Rolleston et al. (2000) (light blue crosses). The green line shows the linear least-squares fit to the measurements: it has a slope of $-0.082 \text{ dex kpc}^{-1}$. The data points have been updated and rescaled to $R_0 = 7.5 \text{ kpc}$ as described in the text. Where necessary points have been shifted vertically by -8.93 to put them on the solar scale.

for a model similar to those presented by Dehnen & Binney (1998) but with the thin and thick disc scaleheights taken to be 0.3 and 0.9 kpc, the total stellar surface density set to $35.5 M_\odot \text{ pc}^{-2}$ with 3/4 of the stellar mass in the thin disc, and the gas surface density set to $13.2 M_\odot \text{ pc}^{-2}$ in conformity with Flynn et al. (2006) and Juric et al. (2008). The disc scalelength is taken to be $R_d = 2.5 \text{ kpc}$ (Robin et al. 2003) and the dark halo density is set such that $v_c(R_0) = 220 \text{ km s}^{-1}$.

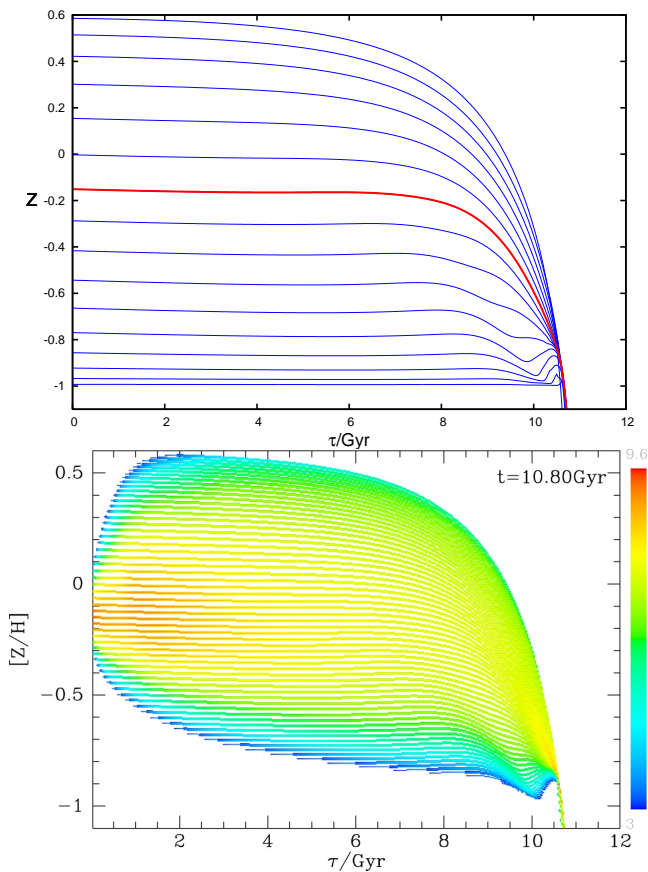


Figure 6. Upper panel: the metallicity of the cold ISM in each annulus as a function of lookback time showing each fifth ring. The curve for the solar annulus is red. Lower panel: the present density of solar-neighbourhood stars in the age-metallicity diagram. The colours encode the logarithm of the density of stars.

3 THE STANDARD MODEL

We now describe the properties of our standard model as a preliminary to explaining how these properties depend on the input assumptions and the values of the various parameters. In the standard model the accretion rate is given by equation (6); the values of the parameters for this model are given in Table 1.

The red dashed curve in Fig. 5 shows the current metallicity Z of the ISM as a function of radius. There is quite a steep outward decline in metallicity with radius, the gradient in the vicinity of the Sun being of order $-0.11 \text{ dex kpc}^{-1}$. For the gradient in general metallicity Holmberg et al. (2007) give a value of $-0.09 \text{ dex kpc}^{-1}$ for a thin disc selection of the GCS data and a simple fit for sample stars with $[Z/H] > -0.7$ (excluding halo objects) yields values of around $-0.11 \text{ dex kpc}^{-1}$. The solid red curve shows that $[O/H]$ falls less steeply with R than does $[Z/H]$, having a gradient near the Sun $\sim -0.083 \text{ dex kpc}^{-1}$. The shallower gradient in oxygen reflects our use of metallicity-dependent yields. Although shallower gradients are generally cited (e.g. Rolleston et al. 2000) the data points in the figure are consistent with the model. The data derive from Shaver et al. (1983) who assumed $R_0 = 10 \text{ kpc}$ and from Vilchez & Esteban (1996) and Rolleston et al. (2000), who

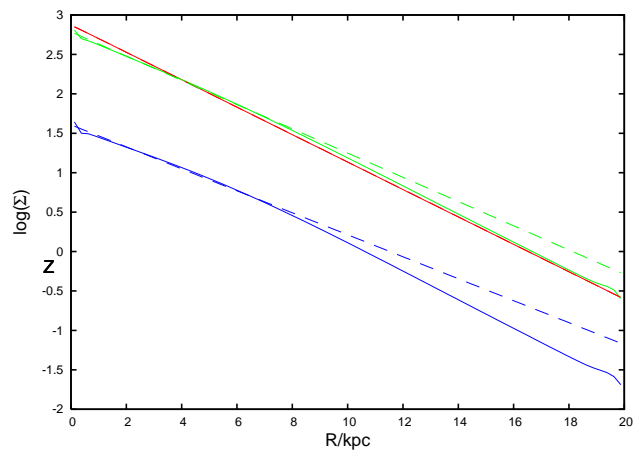


Figure 7. Full green curve: the surface density of the stellar disc at 11.4 Gyr. Broken green line: exponential fit to the inner part of this curve. Red curve: the surface density of stars born in the first 0.8 Gyr. Broken blue line: linear fit to this curve.

assumed $R_0 = 8.5 \text{ kpc}$. To plot these data on a consistent scale with $R_0 = 7.5 \text{ kpc}$ we have when possible recalculated the Galactocentric distances from the heliocentric distances, taking the latter from Kharchenko et al. (2005) or Loktin & Beshenov (2003) when possible. For some of the points in Vilchez & Esteban (1996) and Rolleston et al. (2000) heliocentric distances were not available, so we simply reduced the cited Galactocentric distance by 1 kpc. The green line in Fig. 5 is the linear least-squares fit to the data; its slope is $-0.082 \text{ dex kpc}^{-1}$. Our gradient in $[O/H]$ lies within the range of frequently occurring values in Table 4 of Vila-Costas & Edmunds (1992), who assembled data for 30 disc galaxies.

The upper panel in Fig. 6 shows the evolution of Z for the cold ISM in a number of annuli – the solar annulus is coloured red. The smaller the radius of an annulus, the higher its curve lies in this plot because chemical evolution proceeds fastest and furthest at small radii. At small radii the metallicity of the cold ISM continues to increase throughout the life of the Galaxy, whereas at $R \gtrsim R_0 \text{ kpc}$, Z peaks at a time that moves earlier and earlier as one moves out, and declines briefly before flattening out. This phenomenon reflects a combination of dilution by infalling metal-poor gas and the inward advection of metals by the flow through the disc.

The lower panel in Fig. 6 shows the corresponding present-day metallicity distribution of solar-neighbourhood stars. Although this is the distribution of stars currently in the solar annulus, it is clearly made up of a series of curves, one for each annulus in the model. The curves for interior annuli go from blue to green as one goes back in time, reflecting the fact that relatively recently formed stars are much less likely to have moved a large radial distance than older stars. Similarly, in the bottom part of the figure the colours go from red to green to blue as one moves towards the time axis, because then one is moving over curves for larger and larger radii, where both the star-formation rate and the probability of scattering in to the solar radius are low. Hence, regardless of stellar age, most solar-neighbourhood stars have Z in a comparatively narrow range centred on $[Z/H] \simeq -0.2$.

The full green curve in Fig. 7 shows the surface density

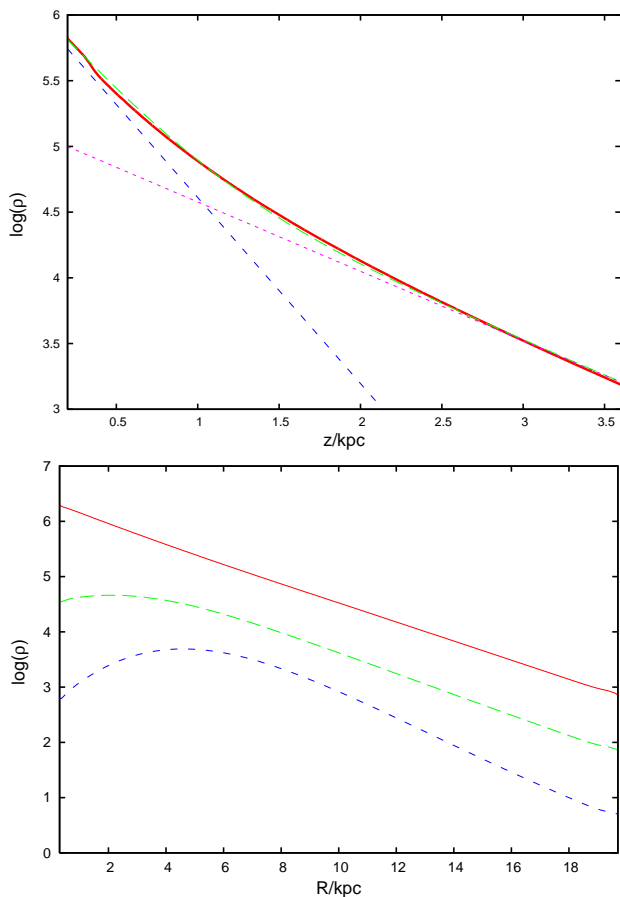


Figure 8. Upper panel: the volume density of stars at $R = 7.6$ kpc as a function of height (red), a fit (green dashed) and its decomposition into thin and thick components. Lower panel: the volume density of stars at the current epoch at $z = 0$ (red), $z = 0.75$ kpc (green dashed) and $z = 1.5$ kpc (blue short dashed).

of the stellar disc at 10 Gyr, which is roughly exponential. The red points show what the surface density would be if stars remained at their radii of birth. By construction this forms an exponential disc with a scalelength of 2.5 kpc. The broken green line shows that at $R < R_0$ the disc approximates an exponential with a larger scale length ~ 2.8 kpc. The blue curve shows the surface density contributed by stars formed in the first 0.8 Gyr, which will be α -enhanced. This distribution deviates more strongly from an exponential because radial migration is most important for old stars. Fitting an exponential to this curve at $R < R_0$ yields a scale-length 3.1 kpc.

Fig. 8 reveals that thin and thick disc components can be identified within this overall envelope: the upper panel shows that the vertical stellar density profile at the Sun is not exponential but can be fitted by a sum of two exponentials. There is significant latitude in these fits and the fraction of stars that is assigned to each component varies with their scalelengths. For comparison with recent results of Juric et al. (2008) we present a fit with their value for the local thick disc fraction of 12 per cent. This yielded scalelengths of $h_1 = 307$ pc and $h_2 = 823$ pc, very well in the range of their results. However, precise characterisation of the vertical structure will not be meaningful until dynamical models are available that employ an accurate form of the third integral of galaxy dynamics.

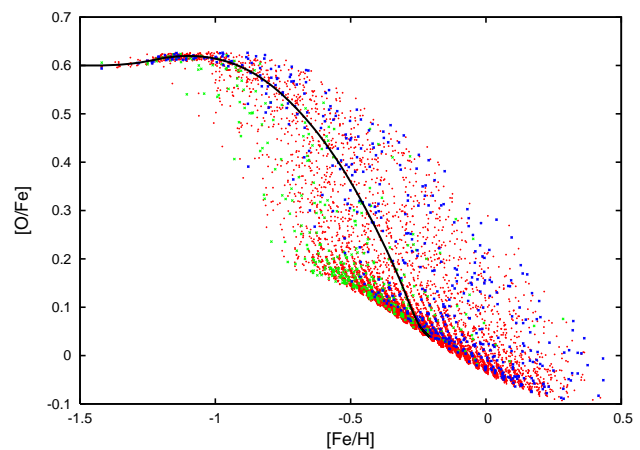


Figure 9. The predicted distribution of solar-neighbourhood stars in the $([\text{Fe}/\text{H}], [\text{O}/\text{Fe}])$ plane. The sample is obtained by using the selection function of the GCS survey as described in Section 4 below and requiring that rotation velocities lie in $(179, 244) \text{ km s}^{-1}$ to ensure that all stars are kinematically thin-disc stars. The colours of points depend on the star's azimuthal velocity: $v_\phi < 179 \text{ km s}^{-1}$ blue; $179 < v_\phi/\text{km s}^{-1} < 244$ red; $v_\phi > 244 \text{ km s}^{-1}$ green. The black curve shows the trajectory of the solar annulus.

ical models are available that employ an accurate form of the third integral of galaxy dynamics.

The lower panel of Fig. 8 shows that at $z = 1.5$ kpc (where the thick disc is dominant) the stellar distribution is less centrally concentrated than it is in the plane; if one were to fit an exponential profile to the stellar density at $z = 1.5$ kpc for $R < 10$ kpc, the scalelength fitted would be larger than that appropriate in the plane. Just this effect is evident in Fig. 16 of Juric et al. (2008).

Fig. 9 shows the predicted distribution of solar-neighbourhood stars in the $([\text{O}/\text{Fe}], [\text{Fe}/\text{H}])$ plane when a sample is assembled using the GCS selection function described in Section 4 below. Two ridge-lines are evident: at top left of the figure a population starts that stays at $[\text{O}/\text{Fe}] \simeq 0.6$ until $[\text{Fe}/\text{H}] \simeq -0.75$ and then turns down towards $(0, 0)$, while a second larger population starts at about $(-0.75, 0.25)$ and drops steeply for $[\text{Fe}/\text{H}] \gtrsim -0.5$. This arrangement of points is very similar to that seen in Fig. 2 of Venn et al. (2004). The upper group is associated with the thick disc, and the lower group with the thin disc. In the appendix we show that such bimodal distributions in $[\text{O}/\text{Fe}]$ are a natural consequence of the standard assumptions about star-formation rates and metal enrichment that we have made. The structure is *not* a particular product of the double-exponential nature of the standard model's infall law; the model with a constant gas mass displays exactly the same structure. Breaks in the Galaxy's star-formation history (Chiappini et al. 1997) and accretion events (Bensby et al. 2005) have been hypothesised to account for the dichotomy between the thin and thick discs. Our models reproduce the dichotomy without a break or other catastrophic event in our model's star-formation history. When comparing Fig. 9 with similar plots for observational samples, it is important to bear in mind differences in selection functions: Fig. 9 is for a kinematically unbiased sample, while

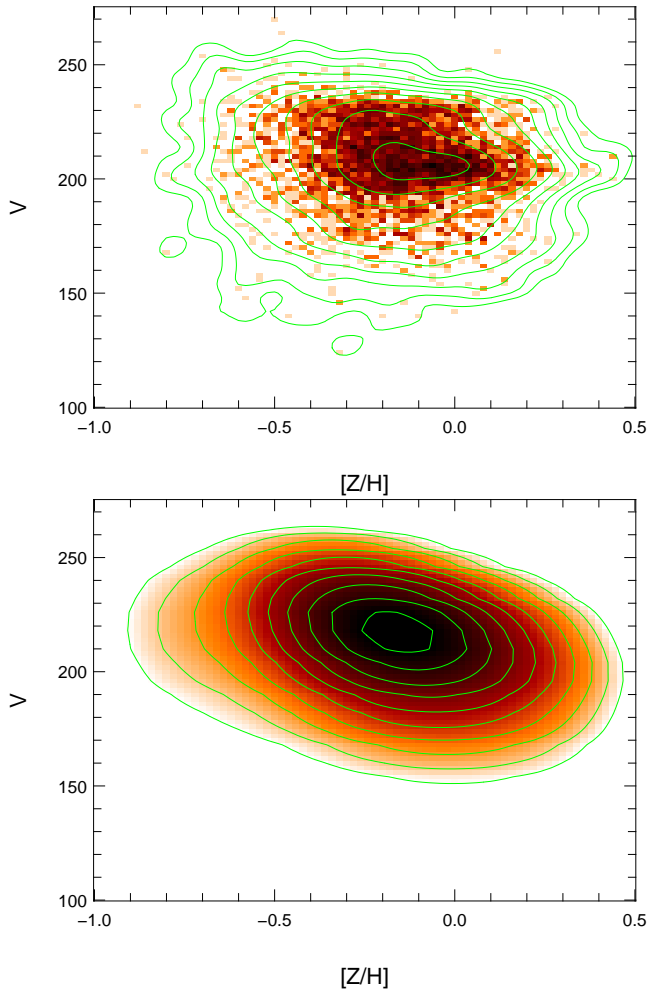


Figure 10. Upper panel: the distribution of GCS stars in the $([Z/H], v_\phi)$ plane. Lower panel: the prediction of the standard model. Colours and contours reflect the density on a logarithmic scale with a 0.2 dex spacing for contours.

most similar observational plots are for samples that are kinematically biased in favour of “thick-disc” stars.

The full curve in Fig. 9 shows the trajectory of the solar-neighbourhood ISM. At low $[\text{Fe}/\text{H}]$ this runs along the ridge line of the thick disc, and it finishes on the ridge line of the thin disc, but it is distinct from both ridge lines. The sharp distinction between this curve and the ridge line of the thin disc make it very clear that the latter is formed through the migration of stars into the solar neighbourhood, *not* through the chemical evolution of the solar neighbourhood itself.

In Fig. 9 the points are colour coded by their angular momenta/guiding centres: blue points are for $v_\phi < 179 \text{ km s}^{-1}$ ($R_g < 0.81 R_0$), red points are for $179 \text{ km s}^{-1} \leq v_\phi \leq 244 \text{ km s}^{-1}$ and green points are for $v_\phi > 244 \text{ km s}^{-1}$ ($R_g > 1.1 R_0$). At the low-metallicity end of the thin-disc ridge line many points are green and few blue, while at the high-metallicity end the reverse is true. Thus low-metallicity thin-disc stars tend to have guiding centres $R_g > R_0$, while high metallicity stars have $R_g < R_0$. Haywood (2008) has noted the same metallicity-velocity correlations in samples of nearby stars. The thick disc contains stars from all three

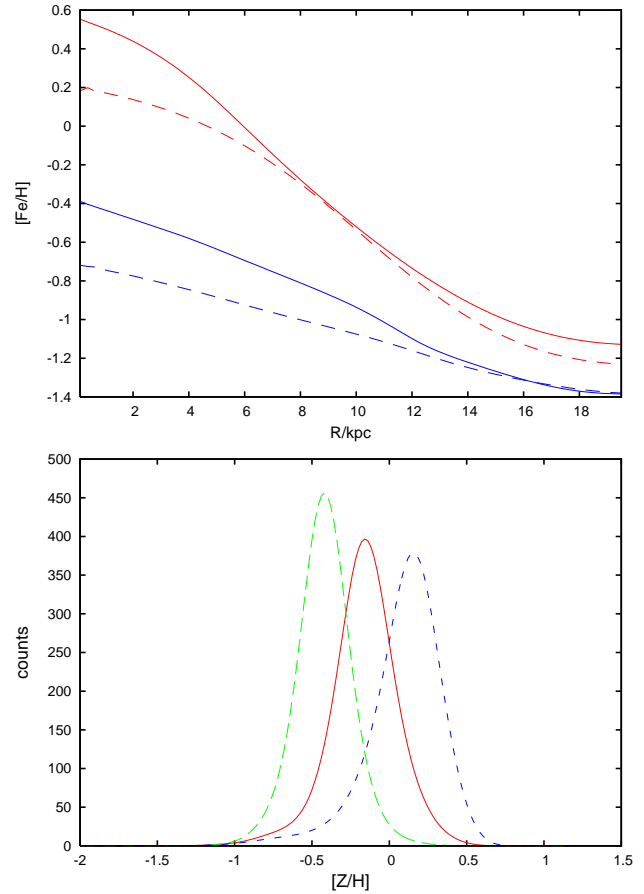


Figure 11. Upper panel: mean metallicities of stars (dashed) and cold ISM (full) as functions of R at the present time (red) and at 1.5 Gyrs (blue). Lower panel: the distributions over metallicity of stars currently at $R = 5 \text{ kpc}$ (blue), 7.6 kpc (red), and 10 kpc (green).

radial ranges, but stars with small R_g (blue) are most prominent at higher $[\text{Fe}/\text{H}]$.

Fig. 10 shows the distribution of stars in the $([Z/H], v_\phi)$ plane. The highest density of stars lies near $(0, 220 \text{ km s}^{-1})$. The vertical extent of the distribution increases as one moves to lower metallicities. The metallicity gradient in the disc leads to the main cluster of stars sloping downwards to the right. This figure invites comparison with Fig. 5 of Haywood (2008). In that figure there is a band of points running from small v_ϕ and $[Z/H]$ up towards the main cluster. This band is made up of halo and thick disc stars that are selected for in the samples from which Haywood drew data. The other difference between Haywood’s Fig. 5 and our Fig. 10 is that Haywood’s main clump has a slightly less pronounced slope down to the right. It is likely that errors in the measurements of $[\text{Fe}/\text{H}]$ have moderated this slope. The GCS distribution shown in the upper panel of Fig. 10 is (especially to the high metallicity side) dominated by overdensities at certain rotational velocities that might be attributed to stellar streams (e.g. the Hercules stream). This pattern overlays the general downwards slope. The model accounts well for the steeper edge of the density distribution on the high rotational velocity side, which is the combined effect of lower inwards blurring and lower stellar densities from outer rings.

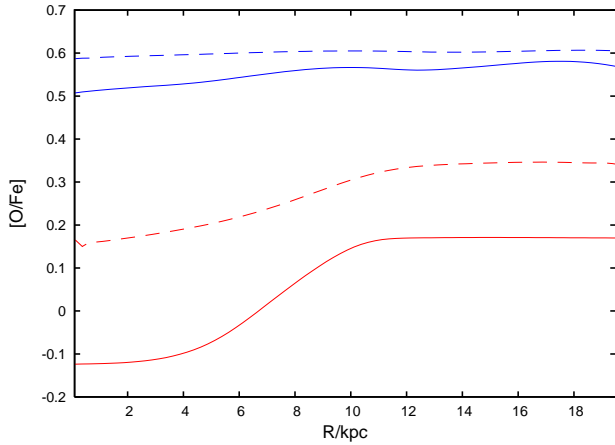


Figure 12. Full lines: $[\text{O}/\text{Fe}]$ in the cold ISM after 1.5 Gyr (blue) and 12 Gyr (red). Dashed lines: Mean $[\text{O}/\text{Fe}]$ of stars after 1.5 Gyr and 12 Gyr.

The top panel of Fig. 11 shows that the stellar metallicity distribution is less centrally concentrated than that of the cold ISM from which stars form. Three factors are responsible for this result. First, the mean metallicity of stars reflects the metallicity of the gas at earlier times, which was lower. This effect is most pronounced at the centre, where the metallicity of the ISM saturates later than further out. Second, radial mixing, which flattens abundance gradients, has a bigger impact on stars than gas because stars experience both churning and blurring. Third, the net inflow of gas steepens the abundance gradient in the gas. The lower panel Fig. 11 shows the breadth of the metallicity distribution at three radii.

Fig. 12 shows how α -enhancement varies in time and space, in stars and gas. Naturally, $[\text{O}/\text{Fe}]$ declines with time in both the ISM and in the stellar population, and at a given time is higher in the stars than the gas. $[\text{O}/\text{Fe}]$ generally increases outwards but at 12 Gyr in both stars and gas it attains a plateau at $R \gtrsim 10$ kpc, with $[\alpha/\text{H}] \sim 0.2$ in the gas. The existence of the plateau is a consequence of the rule that in the IGM $[\text{O}/\text{H}]$ is the current value in the disc at $R \simeq 12$ kpc; gas with the given α -enhancement rains on the disc at $R \lesssim 20$ kpc, is enriched by supernovae of both types and a few gigayears later arrives at $R = 12$ kpc with its original α -enhancement. This level is set by the metallicity-dependent yields we have employed.

Fig. 13 shows the B , R and I -band absolute magnitudes of the standard model as a functions of time. The B -band luminosity rises quickly to a peak at 2 Gyr and then commences a very slow decline. Emissions in the R -Band are almost constant, while I -band luminosities continue to rise throughout the Galaxy's life because fresh additions to the stock of long-lived stars outweigh deaths of relatively short-lived and predominantly blue stars. In our model the Galaxy reaches an I -Band magnitude of around -22.7 which is exactly the result one would expect for a disc galaxy with a rotation velocity of 220 km s^{-1} (e.g. Pizagno et al. 2005)

Fig. 14 shows the $U-B$ and $B-I$ colours of the disc at $t = 1.5, 4.5, 8.4$ and 12 Gyr. As expected, the disc reddens at a declining rate throughout its life. There is at all times a significant colour gradient between $R = 8$ and 16 kpc that

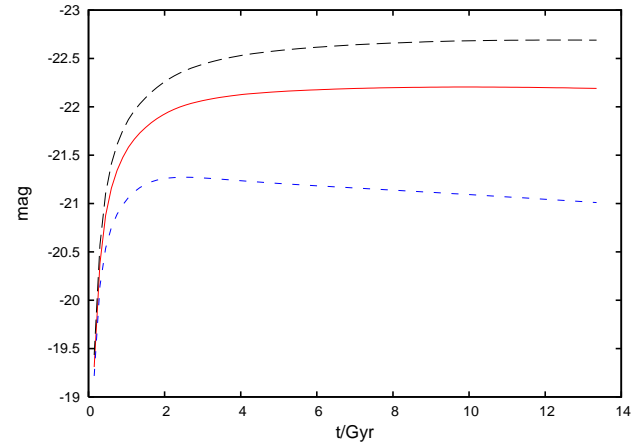


Figure 13. Absolute magnitudes in the B (blue short dashed), R (red) and I (black long dashed) bands as functions of time. No allowance has been made for obscuration.

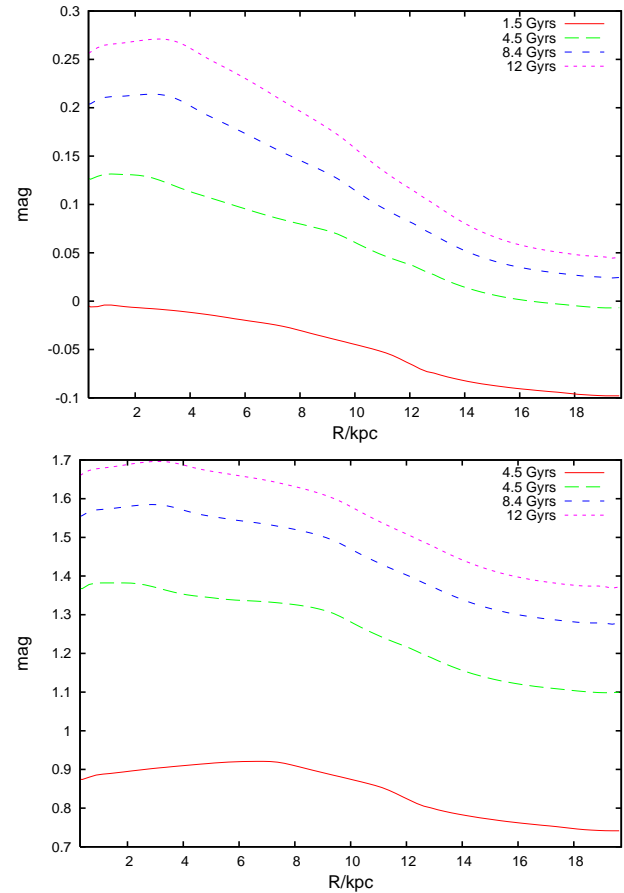


Figure 14. $U-B$ (upper panel) and $B-I$ (lower panel) as functions of radius at $t = 1.5, 4.5, 8.4$ and 12 Gyr. No allowance has been made for obscuration.

make the disc's edge about 0.2 mag bluer in $B-I$ than its centre.

Fig. 15 shows that radial migration causes the dependence of velocity dispersion on time for stars that are currently in the solar neighbourhood to differ materially from the acceleration law (17) that determines the time depen-

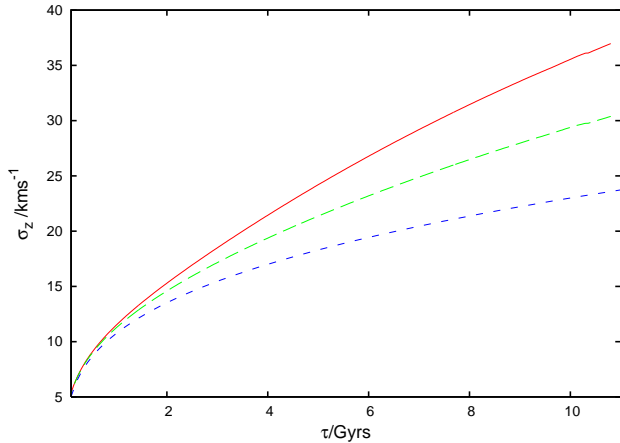


Figure 15. Velocity dispersion of solar-neighbourhood stars as a function of age. Red curve: σ_z for all stars in the solar annulus. Green (long dashed) curve: σ_z for stars within 100 pc of the Sun. Blue (short dashed) curve: σ_z for stars born in the solar annulus.

dence of σ_z for stars that are born at given radius. The outward migration of stars brings to the solar neighbourhood stars that carry with them the large velocity dispersions characteristic of their places of birth. The impact that these migrants have on σ_z for stars of a given age increases with age, so at high ages σ_z increases faster than equation (17) predicts. Least-squares fits of $\sigma_z \propto t^\beta$ to the red and green curves in Fig. 15 yield $\beta = 0.52$ and 0.43 , respectively. Empirically the photometrically complete portion of the Hipparcos catalogue shows that the best power-law fits to the rate of increase of σ_z yield $\beta \simeq 0.45$ (Just & Jahreiss 2007; Aumer & Binney 2008). From a theoretical standpoint, this result has hitherto been puzzling because the largest exponent that can be obtained from the dynamics of star scattering is $1/3$ (Binney & Lacey 1988). Such studies treat the acceleration as a local process. Our result suggests that the conflict between theory and observation is attributable to violation of this assumption.

4 FITTING THE MODEL TO THE SOLAR NEIGHBOURHOOD

A major constraint on the models is provided by comparing the model's predictions with samples of stars observed near the Sun. To make these comparisons, we have to reproduce the selection functions of such samples, which proves a non-trivial job.

The GCS is an important sample, and for each model we calculate the likelihood of this sample. Nordström et al. (2004) obtained Strömgren photometry and radial velocities for a magnitude-limited sample of 16 682 F and G dwarfs, nearly all of which have good Hipparcos parallaxes. From the photometry they estimated metallicities and ages. Haywood (2006) argues that around the turnoff colour for old disc stars the GCS effective temperatures are systematically too low by ~ 100 K. He further argues that at some values of $B - V$ the GCS metallicities are too low by ~ 0.2 dex. In light of these criticisms Holmberg et al. (2007) derived new values of T_{eff} and Z for stars in the GCS sample, but at

Table 2. Magnitudes defining the Geneva–Copenhagen selection function

$b - y$	$0.2 - 0.25$	< 0.344	< 0.38	< 0.42	> 0.42
v_1	7.7	7.8	7.8	7.8	8.2
v_2	8.9	8.9	9.3	9.3	9.9

the time of writing the revised values have not been made available.

The uncertainties in T_{eff} and Z together with additional uncertainties in isochrones, combine to make the ages of individual stars controversial (Haywood 2006). In view of this situation, we do not use individual stellar ages but work with the quantities from which they are derived. Thus the models' predictions for the density of stars in (M_V, T_{eff}, Z) space have been compared with the density of stars in this space derived by Holmberg et al. (2007).

For each metallicity we construct a volume-limited stellar number density of stars in the (M_V, T_{eff}) plane by considering each annulus j , and calculating the fraction of each population in this annulus that will be in the solar neighbourhood. For given absolute magnitude, the probability that a star will enter the sample is

$$W(r_{\text{max}}) = \int_0^{r_{\text{max}}} dr r^2 \int d^2\Omega n(z), \quad (19)$$

where the space density of stars $n(z)$ is assumed to be plane parallel and given by equation (18).

The GCS stars are selected by $b - y$ colour in addition to apparent magnitude. At each colour, the appropriate selection function ϕ is characterised by two apparent magnitudes v_1 and v_2 listed in Table 2: ϕ declines linearly from unity at magnitudes brighter than v_1 to zero fainter than v_2 . ϕ vanishes for $b - y$ bluer than 0.2 and at redder colours the values of ϕ just described are multiplied by 0.25 for $b - y$ in $(0.2, 0.21)$ and by a number that rises linearly to 1 over the interval $(0.21, 0.25)$. For $b - y$ redder than 0.38, ϕ is reduced by a factor 0.4.

Nordström et al. (2004) noted that they had problems with properly determining the parameters of red giants. Since this has led to some serious biases against red giants, we take out of consideration the upper parts of the RGB region, while we downscale the theoretically expected population density near the starting point of the red giant branch by a factor of 4 to reconcile it with the incomplete data. Since the numbers of RGB-stars in the GCS are not large anyway, the loss of information is small. We also removed from the dataset three objects that are far too faint to be attributed to the main sequence. The theoretical distributions are convolved with a Gaussian of dispersion 0.1 dex in $[Z/H]$ to allow for measurement errors.

Fig. 16 compares predicted (lower panel) and observed (upper panel) Hess diagrams for the GCS stars. As discussed by Holmberg et al. (2007), the ridge-line of the main sequence in the GCS data is significantly displaced from that predicted by isochrones. We have eliminated the effects of this offset on Fig. 16 in the simplest possible way, namely by decreasing all model values of $\log(T_{\text{eff}})$ by the value, 0.015, that yields the closest agreement between the theoretical and observation main sequences. After this correction has been made, the agreement between the theoretical and observational Hess diagrams shown in Fig. 16 is convincing

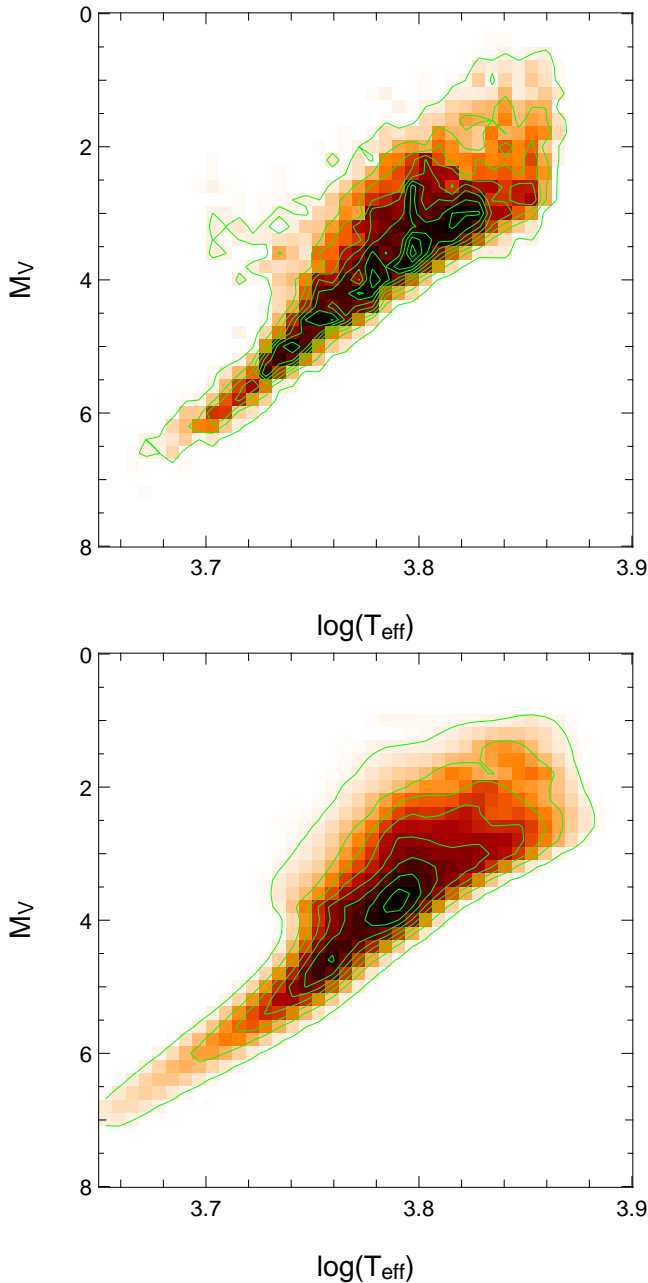


Figure 16. Comparison of the observed (upper) and predicted (lower) distributions of GCS stars in the (T_{eff}, M_V) plane. Contours have an equal spacing of 10 counts per bin, starting with 3.

though not perfect. The original conception had been to determine the model’s parameters by maximising the likelihood of the GCS stars in the model density in (M_V, T_{eff}, Z) space, but confidence in this plan was undermined by (a) the need for an arbitrary alignment of measured and theoretical values of T_{eff} , and (b) the extent to which the likelihood of the data depends on the uncertain GCS selection function. Notwithstanding these reservations, we are encouraged that the standard model maximises the likelihood of the data at an age, ~ 11 Gyr, that agrees with other estimates of the age of the solar neighbourhood (Aumer & Binney 2008).

The pink curve in Fig. 17 shows the metallicity distri-

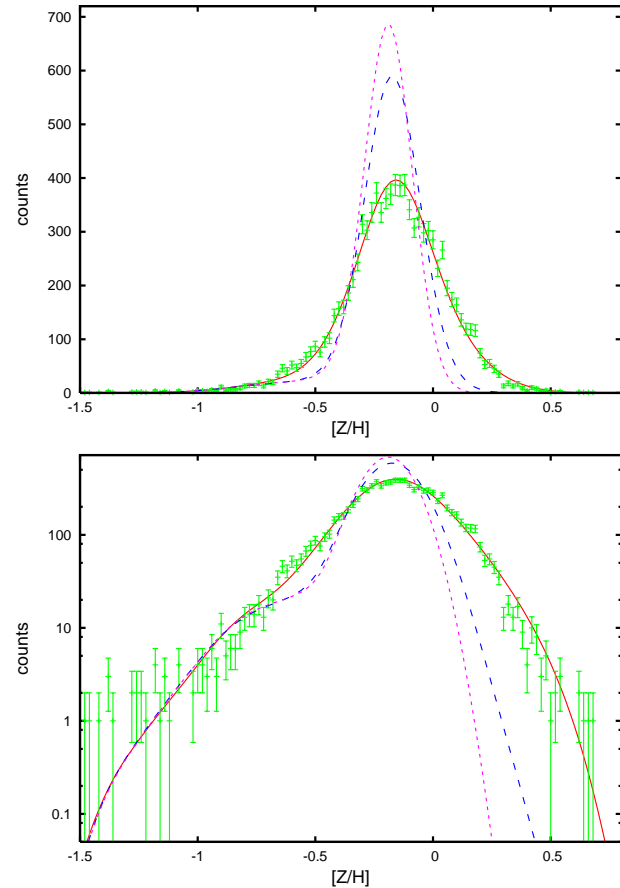


Figure 17. The metallicity distribution of GCS stars (green points) and the corresponding prediction of the standard model (full pink curve). The broken blue curve shows the model that differs from the standard model only in the elimination of churning and radial gas flows. The broken pink curve shows the model with neither churning nor blurring. The lower panel shows the same data but with a logarithmic vertical scale to reveal structure in the wings of the distribution.

bution of stars predicted by the standard model, and green points show the GCS data. The agreement is excellent for $[Z/H] \gtrsim -1.5$. At lower metallicities theory predicts too few stars, but the uncertainties in both the theory and the data are large in this limit. In particular, the theory does not include halo stars, so it should underpredict the data at $[Z/H] \lesssim -1.5$.

5 GENERAL TRENDS

We now discuss aspects of how the observable properties of a model depend on its parameters, and what is required to achieve fits of the quality seen in Figs 6 and 17.

The number of stars more metal poor than $[Z/H] \sim -1$ depends sensitively on the thermal structure of the early ISM. Most previous studies (exceptions include Thomas et al. 1998; Samland & Gerhard 2003) have used only one phase of the ISM. Introducing the warm component of the ISM delays the transfer of metals to the star-forming cold ISM by ~ 1 Gyr, thus increasing the number of extremely metal-poor G dwarfs. Our first models initially had no warm gas,

with the result that at early times the mass of warm gas was proportional to time and the metallicity of the cold gas rose quadratically with time. These models had an overabundance of *very* metal-poor stars. These experiments led to the conclusion that the halo endowed the disc with warm, metal-rich gas at the outset. Even at late times, the existence of the warm ISM delays the introduction of freshly-made metals into stars, and thus in concert with the gas flow through the disc steepens the metallicity gradient in the stars.

The metallicity of infalling gas only affects the structure of the disc at $R \gtrsim 12$ kpc.

It is instructive to consider the case in which blurring is included but churning and radial flows have been turned off ($k_{\text{ch}} = 0$, $f_A = 1$, $f_B = 0$). The broken blue curve in Fig. 17 shows the present-day metallicity distribution that this model predicts for the GCS. The peak of the distribution is much narrower than in the standard model, and there is a striking deficiency of metal-rich stars. The broken pink curve shows the effect of also turning off blurring: the deficiency of metal-rich stars becomes even more striking but there is negligible change on the metal-poor side of the peak.

Slowing the model's SFR by reducing the infall rate shifts the peak of the distribution to lower metallicities by reducing the amount of nucleosynthesis in the solar neighbourhood.

In all interesting models the metallicity of the local ISM saturates early on. The saturation level depends on pattern of gas flow through the disc, and on the current SFR relative to the mean rate in the past: the faster the decline in SFR, the higher the current metallicity. Naturally the stars of the solar neighbourhood are on the average younger in models with a constant gas mass than in models in which the infall rate is declining according to equation (6). This relative youth is reflected in the structure of the local Hess diagram. We reject the model with constant gas mass because it assigns a significantly smaller likelihood to the Hess diagram of the GCS stars than does a model based on equation (6).

5.1 Selecting the standard model

All our models have quite strong metallicity gradients in both stars and gas (Fig. 5). Since the metallicity of the central gas is enhanced by radial gas flow, and models with large f_B have larger central flows than models with large f_A and vice versa at large radii (Fig. 2), enhancing f_B steepens the metallicity gradient at small R and diminishes it at large R .

Eliminating churning and radial gas flows (by setting $k_{\text{ch}} = 0$, $f_A = 1$, $f_B = 0$) dramatically reduces the metallicity gradient within both the stellar and gas discs: at the present epoch the gradient in the gas near the Sun falls from $-0.11 \text{ dex kpc}^{-1}$ to $-0.01 \text{ dex kpc}^{-1}$. Increasing the churning amplitude k_{ch} both increases the width of the peak in the predicted solar-neighbourhood metallicity distribution (Fig. 17) and reduces the gradient in the mean metallicity of stars at $R \lesssim R_0$.

Fig. 18 shows how the likelihood of the GCS metallicity distribution plotted in Fig. 17 varies with f_A , f_B and k_{ch} . In the upper panel favoured models (with large symbols) lie along a line that slopes down and to the right. Along this line a decrease by 0.01 in f_B is compensated by an increase

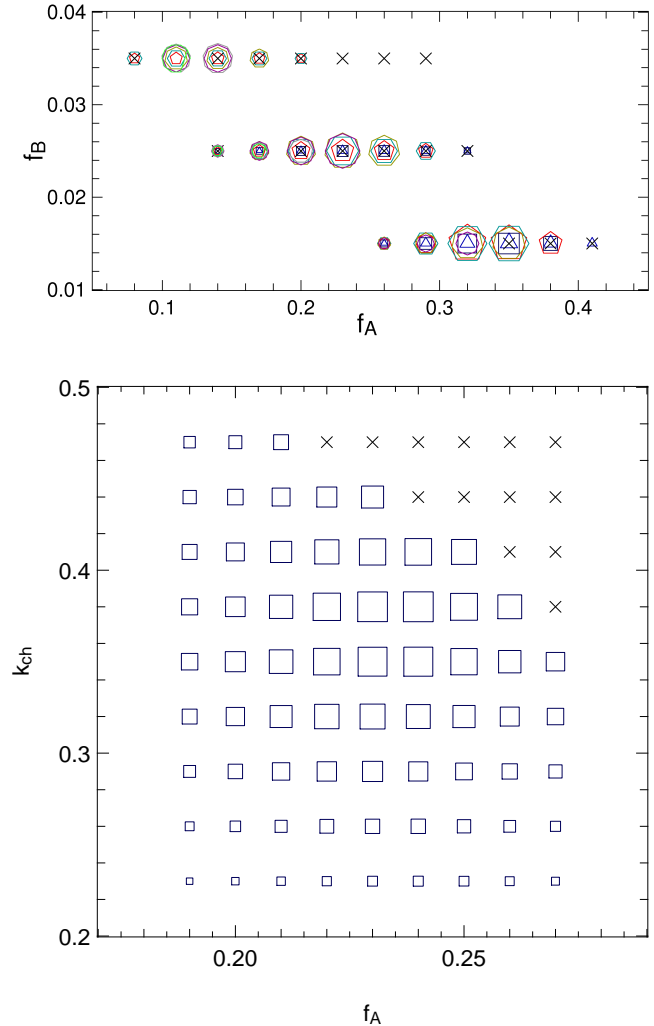


Figure 18. The likelihood of the GCS metallicity distribution in models with infall rates given by equation (6). Upper panel: the values of the infall parameters f_A and f_B are given by the locations of the symbols, and the value of k_{ch} is indicated by the number of sides of the polygon: 3, 4, 5, ... for $k_{\text{ch}} = 0.25, 0.3, 0.35, \dots$. The size of the polygon increases linearly with the log likelihood of the data. Lower panel: the likelihoods of models with $f_B = 0.025$ and varying (f_A, k_{ch}) . In this panel the size of a symbol is a more sensitive function of likelihood than in the upper panel. In both panels a cross rather than a polygon is drawn when the time yielding the largest likelihood is smaller than 9 Gyr.

in f_A by ~ 0.08 . The similar sizes of the triangles, squares, etc., along this line indicates that the fit is not sensitive to k_{ch} .

As one moves down the upper panel of Fig. 18, the steepness of the metallicity gradient near the Sun increases, and the models with $f_B = 0.015$ have local gradients steeper than $-0.12 \text{ dex kpc}^{-1}$, which may conflict with the data. Models higher up the panel have smaller local metallicity gradients and require larger values of k_{ch} to bring a sufficient variety of stars to the solar neighbourhood. Models to the right of the panel have smaller inward flows of gas, leading to local metallicities that rise faster in time and they match the GCS metallicity distribution at younger ages, especially if k_{ch} is large so metal-rich stars migrate to the Sun

relatively rapidly. The structure of the local Hess diagram for either GCS stars (Fig. 16) or Hipparcos stars (Aumer & Binney 2008) implies that the solar neighbourhood is not younger than 9 Gyr, so when the age is smaller than 9 Gyr the model is marked by a cross in Fig. 18. Models adjacent to the crosses do not violate the 9 Gyr limit but are nonetheless disfavoured because their local Hess diagrams yield relatively low likelihoods for the GCS sample.

Four factors make it difficult to confine narrowly the required value of k_{ch} within the part of Fig. 18 that has large symbols: (i) churning affects mainly the width of the metallicity distribution, which has less impact on the likelihood than the location of its peak; (ii) churning, which is strongest in the inner regions of the disc, tends to saturate near the centre in the sense that old stars become fully shuffled; (iii) the GCS sample is biased against old stars, so where churning has the strongest effect, the observational signature is weak; (iv) the required churning strength is very sensitive to the local metallicity gradient which is not very well constrained by observations.

In our models there is no azimuthal variation in the metallicity of gas at a given radius. The effect of relaxing this assumption can be gauged by increasing the dispersion in the measured metallicities of a given population of stars: if there is intrinsic dispersion in the metallicity of the ISM in a given annulus, the measured metallicities of stars formed from it will reflect both this dispersion and measurement errors. The largest intrinsic dispersion in the metallicity of the ISM that would appear to be compatible with the data plotted in Fig. 5 is ~ 0.1 dex. When we combine this with 0.1 dex measurement errors, it proves possible to obtain an equivalent fit to the GCS data of Fig. 17 than that provided by the standard model. In this fit the increased dispersion in the measured metallicities of stars is offset by k_{ch} falling from 0.35 to ~ 0.2 .

We have studied models with several values of the mass-loss parameter f_{eject} and concluded that up to the largest values studied ($f_{\text{eject}} = 0.15$ at $R < 3.5$ kpc and 0.05 elsewhere) f_{eject} does not have a large effect on the model's observable properties, and is anyway degenerate with the still uncertain nucleosynthetic yields. However, increasing f_{eject} makes it slightly easier to find an acceptable model, reflecting the fact that the yields we are using lie at the upper limit of the yields that are consistent with measured metallicities.

The upper panel of Fig. 19 shows the effect on the fit to the GCS metallicity distribution of using a non-zero value of the threshold gas density, Σ_{crit} , below which the SFR declines steeply. Raising Σ_{crit} from zero to $2.5 \text{ M}_{\odot} \text{ pc}^{-2}$ changes the model prediction from the red curve of the standard model to the blue curve; the distribution is now wider and peaks at lower metallicities. The pink dotted curve shows the result of maximising the likelihood of the data subject to the constraint $\Sigma_{\text{crit}} = 2.5 \text{ M}_{\odot} \text{ pc}^{-2}$. In this model f_{A} is increased (to 0.31) and k_{ch} is decreased (to 0.29) relative to the standard model. The new model provides a slightly better fit to the GCS data than the standard model, but, as the lower panel reveals, there is a problem with using a non-zero value of Σ_{crit} : with no star-formation in the outer disc, the metallicity of the ISM becomes constant at the intergalactic value at all large radii. The data show no sign of this plateau, and are probably incompatible with a plateau as low as $[Z/H] = -1$. Values of $\Sigma_{\text{crit}} > 2.5 \text{ M}_{\odot} \text{ pc}^{-2}$

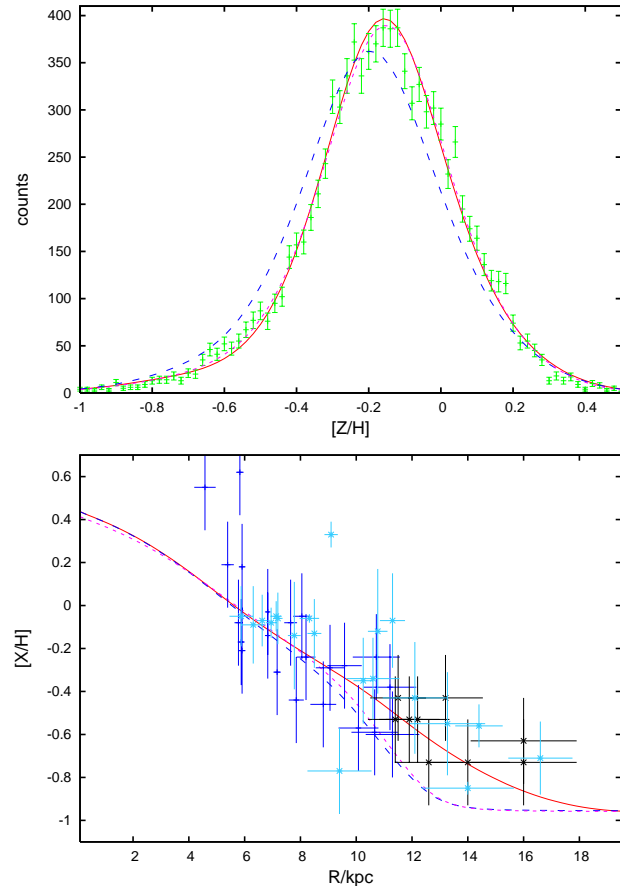


Figure 19. Upper panel: the data points are the GCS counts and the red curve is the standard model. The broken blue curve shows the effect on this model of raising Σ_{crit} from zero to $2.5 \text{ M}_{\odot} \text{ pc}^{-2}$. The pink dotted curve shows that a good fit to the data can be obtained for this value of Σ_{crit} . Lower panel: measurements of the metallicity of the ISM and the predictions of the models shown above.

are incompatible with the data because they bring the edge of the star-forming disc too close to the Sun.

By considering the likelihoods of both the Hess diagram and the metallicity distribution of GCS stars, and our prejudices regarding the proper value of f_{eject} , we chose the model specified by Table 1 as the standard model. With this model the likelihood of the GCS metallicity peaks at age 10.2 Gyr. A slightly better fit to the GCS metallicity distribution can be obtained with a smaller value of f_{B} (more stars at $[Z/H] = -0.6$ and fewer stars at $[Z/H] = 0.4$) at the price of a larger local metallicity gradient in the ISM.

6 RELATION TO OTHER WORK

Chemical evolution models of the Galaxy have a long history and a large literature, and we can only compare our results to a very small number of previous works. Our work is a development of the classical tradition of Galaxy modelling that goes back to van den Bergh (1962) and Schmidt (1963). More ambitious models in which N bodies are used to model the dynamics of dark matter, stars and gas in full while semi-analytic prescriptions follow stellar evolution and nu-

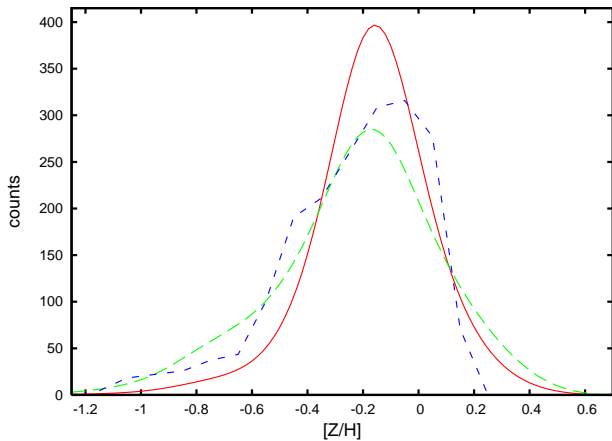


Figure 20. Full red curve: the metallicity distribution predicted by the standard model for the GCS stars. Long-dashed green curve: the prediction of the same model for the distribution of the whole solar annulus. Short-dashed blue curve: the prediction of Chiappini et al. (1997) for the solar annulus.

cleosynthesis, were pioneered by Samland & Gerhard (2003). Such models probably represent the long-term future of the subject, but they are inevitably extremely costly computationally and struggle to achieve the desired resolution in the small patch of the Galaxy that we can study in exquisite detail. Therefore we have thought it worthwhile to develop further the classical modelling tradition.

Within this tradition reference should be made to Chiappini et al. (1997) and its successors Chiappini et al. (2001) and Colavitti et al (2008). In each case the disc is made up of annuli that exchange neither stars nor gas. Star-formation is driven by a Kennicutt law similar to equation (1). Chiappini et al. (1997) introduced a time-dependent infall rate that is superficially similar to (6) but differs from our infall rate in two important respects. First, the exponential with the longer time-constant is not turned on until 2 Gyr after the start of Galaxy formation with the consequence that star formation periodically ceases during the interval $1 \text{ Gyr} < t < 2 \text{ Gyr}$. Second, Chiappini et al. (1997) make the time constant b_2 a linearly increasing function of radius that vanishes at $R = 0.86 \text{ kpc}$ (or 1.2 kpc in Chiappini et al. 2001), whereas here b_2 is constant. If we were to follow the prescription of Chiappini et al., our inner disc/bulge would become older, and a smaller churning rate would be required to bring stars more metal-rich than the local ISM to the solar neighbourhood. An outwards-increasing infall timescale enhances the metallicity gradient because metallicities are close to their equilibrium values, and these reflect the ratio of current to past SFRs.

Chiappini et al. (1997) adjusted their model's free parameters to optimise its fit to the G-dwarf metallicity distribution for stars in the solar annulus that was determined by Rocha-Pinto & Maciel (1996) from 287 stars that lie within 25 pc of the Sun. Fig. 20 illustrates the difference between the metallicity distributions of stars near the Sun and in the entire solar annulus: the full red curve shows the standard model's prediction for the metallicity distribution of GCS stars from Fig. 17, while the long-dashed green curve shows the corresponding distribution in the whole annulus. The distribution for the annulus is much broader than that for

the GCS because stars with metallicities far from that of the local ISM are typically fast-moving and likely to be at high z . Rocha-Pinto & Maciel (1996) transformed their measured distribution for the local sphere to the modelled global distribution using correction factors estimated by Sommer-Larsen (1991), which depend on the local gravitational potential and the velocity distributions of stars of each metallicity. It is clearly more satisfactory to use internally generated values of these distributions to predict the metallicity distribution in the observed volume around the Sun than to infer the annular distribution from the measured one using external estimates of the velocity distributions. Moreover, the short-dashed blue curve in Fig. 20 shows the prediction of Chiappini et al. (1997) for the solar annulus. It is significantly less broad than the blue curve, showing a clear deficit of metal-rich stars.

The scale of the discrepancy between the blue and the green curves illustrates that a model that provides an adequate fit to the data of Rocha-Pinto & Maciel (1996) must be incompatible with the GCS stars. The GCS sample is 100 times larger than that used by Rocha-Pinto & Maciel (1996), so its statistical errors are much smaller and it is a more challenging distribution to fit.

In the models of Chiappini et al. (1997), star formation ceases entirely when the surface density of gas falls below Σ_{crit} , while in our models Σ_{crit} merely marks an increase in the rate of decline of the SFR with decreasing gas density. While a cogent argument can be made for a rapid decline in the SFR at low gas densities, it is hard to justify a discontinuity in the rate. Chiappini et al. (2001) conclude that a non-negligible value of Σ_{crit} plays an essential role in fitting the data. In fact, they set $\Sigma_{\text{cr}} = 7 M_{\odot} \text{ pc}^{-2}$, with the consequence that star formation in the solar neighbourhood was constantly stopping and starting, both during the first 2 Gyr and the last 4 Gyr of Galactic history (see their Fig. 4). We find this behaviour implausible. In our models setting $\Sigma_{\text{crit}} = 7 M_{\odot} \text{ pc}^{-2}$ would result in almost no stars forming at $R \gtrsim 10 \text{ kpc}$ because when star formation cuts off in an annulus, the gas density does not simply rise until Σ_{crit} is reached, as it does in the models of Chiappini et al. (1997). In fact, even with no star formation, the flow of gas through the disc limits the increase in the gas density. Hence at large radii star-formation can occur only if Σ_{crit} is set to a small or vanishing value. For this reason we favour such values.

Chiappini et al. (1997) give for the inner and outer parts of their models the radial gradients in the abundances of several elements. These gradients are largest in the inner regions, but even there they are much smaller than in our models: for example at 12 Gyr the inner gradients of $[\text{O}/\text{H}]$ and $[\text{Fe}/\text{H}]$ are -0.023 and $-0.027 \text{ dex kpc}^{-1}$ compared to values $\sim -0.08 \text{ dex kpc}^{-1}$ and $\sim -0.11 \text{ dex kpc}^{-1}$ obtained here. Our larger gradients are a direct consequence of the advection inwards of the products of nucleosynthesis. The GCS stars show a similar gradient in $[\text{Z}/\text{H}]$: Holmberg et al. (2007) derive a gradient of $-0.09 \text{ dex kpc}^{-1}$.

Colavitti et al (2008) used infall rates measured from simulations of clustering cold dark matter (CDM) in slightly updated version models of Chiappini et al. (1997). No empirically determined infall rate gave such satisfactory results as the earlier double-exponential rate. The models were again compared to the metallicity distribution of Rocha-Pinto & Maciel (1996) and in most cases provided inadequate fits to

the data. The empirically measured infall rates are very irregular in time, with the result that the model experiences powerful bursts of star formation. These lead to large excursions in the predicted plots of $[\text{O}/\text{Fe}]$ versus $[\text{Fe}/\text{H}]$ for which there is no evidence in the data. Moreover, studies of the past SFR in the disc show no signs of major bursts of star formation a few gigayears ago. The disappointing results of this study suggest that the rate at which gas joins the disc is not simply the ratio of masses of baryons and dark-matter times the dark-matter accretion rate. In fact, the wealth of evidence that the majority of baryons are still in the intergalactic medium (Fukigita et al. 1998) is a clear indication that galaxies do not acquire gas as fast as this naive calculation suggests; rather gas is stored in the warm-hot intergalactic medium (WHIM) and from there accreted at a still uncertain rate.

Naab & Ostriker (2006) determined the infall rate by assuming that the surface density of the disc is always exponential, but with a scale length that is proportional to v_c/H , where v_c is the Galaxy's circular speed (taken to be constant) and $H(t)$ is the Hubble parameter. The infall rate at all times and places was fixed by assuming that the central surface density of the disc is constant at its current value. The model's observables were calculated by using the Kennicutt law (1) to convert gas to stars. A very simple approach to chemical evolution was employed, in which material does not move between annuli and only the overall metal content Z was followed. In these models the metallicity gradient in the ISM becomes less steep over time, and is now $\sim -0.04 \text{ dex kpc}^{-1}$. Their model predicts for the solar neighbourhood fewer metal-rich stars and more metal-poor stars than are in the GCS.

In all these models, solar-neighbourhood stars should satisfy a well defined metallicity-age relation, and the G-dwarf metallicity distribution is simply the result of combining this relation with the SFR-age relation.

Haywood (2006) has critically re-examined the age-metallicity distribution of the GCS stars and concluded that the data are only consistent with the existence of a well defined age-metallicity relation for disc stars younger than $\sim 3 \text{ Gyr}$; for such young stars the spread in $[\text{Fe}/\text{H}]$ is consistent with the expected dispersion in the metallicity of interstellar gas at a given radius. At ages larger than 3 Gyr the width of the metallicity distribution is larger than can be accounted for by measurement errors and inhomogeneity of the ISM. In particular, there are stars with ages $\sim 5 \text{ Gyr}$ that have $[\text{Fe}/\text{H}] = 0.5$, and stars with ages $< 7 \text{ Gyr}$ that have $[\text{Fe}/\text{H}] = -0.5$. The older the age bracket that one examines, the wider the range of metallicities present. Our predicted age-metallicity distribution (Fig. 6) is in good agreement with that derived by Haywood (2006).

Haywood (2006) finds that when his revised ages are used for GCS stars, the metallicities of thick disc stars increase as their ages decrease. That is, these stars point to rapid self-enrichment of the thick disc. In fact, Haywood argues that the thick disc is not the relic of some captured satellite(s) but an integral part of the Galaxy's disc and has played a central role in the chemical evolution of the thin disc. Chemical evolution models should treat the disc as a whole, not just individual parts. Our results strongly underline this conclusion from a theoretical perspective. The metallicity-age plot shown in Fig. 1(b) of Haywood (2008)

is satisfyingly similar to the lower panel of our Fig. 6: in both figures the stellar density is highest around $(-0.1, 3)$ and in this region the ridge line gradually drops to the right. At older ages the distributions become broader, being confined by $[\text{Fe}/\text{H}] \sim 0.4$ and -0.5 . At ages greater than 10 Gyr both distributions reach down to $[\text{Fe}/\text{H}] = -1$. In fact the small differences between our figure and that of Haywood are readily accounted for by the substantial errors in measured stellar ages. This fit is remarkable because the model parameters were chosen without reference to measured stellar ages.

An argument sometimes advanced for a dichotomy between the thick and thin discs is the existence of two sequences in the $([\alpha/\text{Fe}], [\text{Fe}/\text{H}])$ plane (Fig. 9). This diagram suggests that the last thick-disc stars to form had higher abundances than the first thin-disc stars to form. To explain this finding in the context of a conventional chemical-evolution model, sudden dilution of the ISM by a massive gas-rich accretion is required (Bensby et al. 2005; Reddy et al. 2006). Against this proposal Haywood (2006) objects that the bulk of the oldest thin-disc stars have $[\text{Fe}/\text{H}] \simeq -0.2$ and there is no evidence that the most metal-poor thin-disc stars are particularly old. Our models show that the observed structure of the $([\alpha/\text{Fe}], [\text{Fe}/\text{H}])$ arises naturally when radial migration is allowed. Haywood (2008) examined the orbital parameters of stars of various metallicities and showed that local thin-disc stars with metallicities that overlap the metallicity range of the thick disc have higher angular momenta than more typical thin-disc stars. Similarly, he found that stars in the high-metallicity tail of the local metallicity distribution have low angular momenta. Our models reproduce these correlations (Figs 9 and 10), which show that radial migration through blurring rather than churning is largely responsible for the presence of these chemically anomalous stars near the Sun.

7 CONCLUSIONS

It is now more than forty years since the theory of stellar evolution attained the level at which it became possible to model the chemical enrichment of the ISM. From the beginning of that endeavour measurements of the abundances of individual solar-neighbourhood stars have played a key role because a star preserves like a time capsule the state of the ISM at the remote epoch of its formation. Considerable theoretical and observational efforts have been devoted to probing the history of the Galaxy with this connection.

Half a century ago, Roman (1950, 1954) and others discovered the connection between the kinematics and chemistry of stars, yet curiously little has been done to include kinematics in models of chemical evolution. The general presumption has been that each annulus of the disc evolves independently of others, and the well-known correlations between chemistry and kinematics can be understood as arising through the stochastic acceleration of stars: older stars tend to have larger random velocities and lower metallicities. No effort was made to develop greater diagnostic power by simultaneously modelling chemistry and kinematics.

The continued use of mutually independent annuli by modellers of chemical evolution is surprising given that it was from the outset recognised that many stars are on signif-

icantly non-circular orbits that each radial half-period cover more than a kiloparsec in radius. In fact, it has generally been assumed that the radial velocity dispersion within the disc rises as one moves inward to values that lead to radial excursions of several kiloparsecs (see Fig. 4). Moreover, observations have long indicated that galactic discs have significant metallicity gradients (e.g. Vila-Costas & Edmunds 1992; de Jong 1996), so radial migration of stars is bound to leave a signature on the metallicity distribution of solar-neighbourhood stars. We have called this aspect of radial migration “blurring”.

The present study owes its impetus to the discovery by Sellwood & Binney (2002) that radial migration is a more potent process than mere blurring: the dominant effect of transient spiral arms is not to heat the stellar disc as had been supposed, but to cause stars either side of corotation to change places without moving to eccentric orbits (“churning”). Since this aspect of spiral structure can *only* be probed through its impact on chemical evolution, we wanted chemical-evolution models that included churning, and logically it was natural to extend these models to include both blurring and radial gas flows.

The only new ingredient to our modelling that might be controversial is the introduction of radial gas flows. Sellwood & Binney (2002) did not demonstrate that gas participates in churning, but they argued that it must on dynamical grounds, and Roskar et al. (2008) found evidence that this was the case in their N-body–SPH simulations of galaxy formation. Less well supported are the inward flows of gas through the disc that are generated by our Schemes A and B for handling accretion. However, as gas streams through spiral arms it dissipates energy in shocks that is ultimately gravitational energy that becomes free as the gas surrenders angular momentum to the stars and drifts inwards. Hence at some level inward gas flows are mandatory. We have no convincing arguments for the particular method of generating flows that we have used. The most we can say is that it is a flexible parametrisation that enables us to form exponential discs for a variety of different assumptions about the radial density of infalling gas. It is evident that if discs are to be exponential, variations in the radial profile of infall must be compensated by flows within the disc. We have absolutely no reason to expect that the infall profile is exponential.

The impact that radial migration has on the local metallicity distribution obviously varies with the magnitude of the metallicity gradient in the ISM, which in turn depends on the gas flow within the disc and therefore the radial infall profile. For this reason the most important parameters of our models are k_A and f_B , which control the distribution of infalling gas.

Unfortunately comparisons between the models and the data are not as clear cut as one would wish on account of systematic uncertainties in the selection function of the GCS stars and the values of T_{eff} and age for individual stars. However, within these uncertainties the models provide acceptable fits to the GCS counts of stars as functions of $[\text{Fe}/\text{H}]$, M_V , T_{eff} and stellar age, as well as reproducing the correlations between tangential velocity and abundance patterns that have been pointed out by Haywood (2008). These fits are achieved by churning, blurring and radial flows working together. They depend on the existence of an appreciable metallicity gradient in the ISM, which is established by the

radial flow of gas, and they depend on radial mixing of stars by blurring and churning. The steeper the metallicity gradient in the gas, the smaller the effect of churning can be, but for any observationally consistent metallicity gradient, churning has a non-negligible role to play.

The models describe the coevolution of the thick and thin discs, and presume that thick-disc stars were formed in the Galaxy rather than accreted from outside. Given the simplicity of our assumptions, the extent to which a dichotomy between an α -enhanced thick disc and a solar-type thin disc automatically manifests itself in the models is remarkable. In particular, in the solar annulus the distributions of $[\text{O}/\text{H}]$ at given $[\text{Fe}/\text{H}]$ are bimodal in the range of $[\text{Fe}/\text{H}]$ associated with the overlap of the two discs (Fig. 9), the vertical density profile can be represented at the sum of two exponentials, and at $R < R_0$ the radial density profile becomes flatter at larger distances from the plane (Fig. 8). None of these characteristics is dependent on our choice of a double exponential for the time dependence of infall: a model in which the gaseous mass, and therefore star-formation rate, is held constant also has these features. They are consequences of the ~ 1 Gyr timescale of type Ia supernovae and the secular heating and churning of the disc.

The models assume that scattering of stars increases the velocity dispersion of a coeval population as $t^{1/3}$, but the models go on to predict that within the solar neighbourhood velocity dispersion increases as a higher power of age, roughly $t^{0.45}$ in agreement with what is found from Hipparcos stars with good parallaxes. This finding may reconcile scattering theory, which cannot readily explain an exponent in excess of $1/3$, with observations. The key point is that radial mixing brings to the solar neighbourhood stars born at small radii, where the velocity dispersion is undoubtedly large.

We find that the nucleosynthetic yields from each generation of stars are still significantly uncertain. Our philosophy has been to use the best values we can find rather than exploit uncertainties in the yields to tune the models to the data. The yields we are using are at the upper limit of those that can provide adequate fits to the data, with the consequence that increasing the value of the mass-loss parameter f_{eject} , which is degenerate with the magnitude of the yields, make it easier to fit the data. Our yields are surely not exactly right and consequently some of the properties the models derive from them will be in error.

The discovery that three-dimensional, non-equilibrium models of the solar atmosphere require the metal abundance of the Sun to be $Z_{\odot} = 0.012 - 0.014$ (Grevesse et al. 2007) poses a major problem for this field. A prerequisite for successful chemical modelling is a consistent metallicity scale for both stars and the ISM. At present the only consistent scale is the traditional one on which $Z_{\odot} = 0.019$, so this is the one we have used.

If a new scale were established on which all metallicities were significantly lower, viable models could be produced by lowering the yields. A straightforward way to do this would be to lower the maximum mass in the IMF: reducing this mass from $100 M_{\odot}$ to $50 M_{\odot}$ would reduce yields by ~ 30 percent in line with the proposed reduction in Z_{\odot} . The oxygen yield would come down fastest, reducing $[\text{O}/\text{Fe}]$ by ~ 0.2 dex.

Although we believe that this study represents a signif-

icant advance on all previous models of Galactic chemical evolution, it is highly imperfect. Some major weaknesses of our work are the following.

1. We have assumed that the probability of mass interchange between rings is proportional to the product of the rings' masses. This probability reflects the number and intensity of spiral feature with corotation at that radius, and should be a function of both mass and velocity dispersion. A further study of self-gravitating discs similar to that of Sellwood & Binney (2002) would be necessary to determine this function.

2. We have assumed that the vertical and radial motions of stars decouple. This assumption has a significant impact on both the relation between age and velocity dispersion in the solar neighbourhood and on the predicted vertical density profile in the solar annulus, which is interesting in itself and impacts on the selection function of GCS stars and thus on our choice of standard model. It is unjustifiable for stars on eccentric orbits, which do play an important role in the model fits. Unfortunately, a sounder treatment is impossible until a better approximation to the third integral of Galactic dynamics is available. It is our intention to resolve this problem through "torus modelling" (e.g. McMillan & Binney 2008).

3. Our models include radial mixing of gas through churning and viscous inspiralling, but do not include radial redistribution of gas by the Galactic fountain (e.g. Benjamin & Danly 1997). A significant body of evidence indicates that star formation drives neutral hydrogen to kiloparsec heights above the plane. NGC 891, which is not dissimilar to the Galaxy, has ~ 25 per cent of its neutral hydrogen more than 1 kpc from the plane (Oosterloo et al. 2007). This extraplanar gas must move over the plane on nearly ballistic trajectories, and in the absence of interaction with the corona (gas at the Galaxy's virial temperature $\sim 2 \times 10^6$ K), the gas must return to the plane further out than its point of ejection. However, observations suggest that neutral gas above the plane is actually flowing inward rather than outward, presumable as a result of interaction with the corona (Fraternali & Binney 2008). The mass of extraplanar gas is so large and the timescale for its return to the plane so short that whichever way this gas flows, it has a considerable potential for radially redistributing metals. Extraplanar gas must be ejected from the disc by supernova-heated gas that is probably highly metal-rich. Some of this gas will be lost to the Galaxy as we have assumed, but some of it will return to the plane with infalling gas. Again there is potential here for significant radial redistribution of metals that has been ignored in the present study.

4. Our treatment of the inner Galaxy is unacceptably crude in that we have replaced the bar/bulge with a disc. Unfortunately introducing the bar opens a Pandora's box of complexities, and at the present time is probably only feasible in the context of a particle-based model such as that of Samland & Gerhard (2003). Our hope is that our imaginary central disc has a similar impact on the chemodynamical state of the local disc to the combined impact of the giant star-forming ring at $R \simeq 4$ kpc, the gas-deficient region interior to this ring and the star-forming x_2 disc at $R \lesssim 200$ pc.

From this list of shortcomings of our models it is clear that we are still far from a definitive account of the Galaxy's

chemical evolution. We shall be satisfied if we have convinced the reader that the interplay between dynamics and chemistry is so tight as to be indissoluble. This fact is at one level inconvenient because it undermines the value of conclusions drawn from traditional models of chemical evolution. But at another level it represents an opportunity to learn more. The connection between the kinematics of stars and the compositions of stars and gas, which can be measured in great detail, involves three areas about which we are too ignorant: the distribution of dark matter within and around the Galaxy, the Galaxy's history of assembly, and the nature of the Local Group's IGM. By building dynamical models of the Galaxy that have chemical evolution built in to the basic structure, we should be able to make decisive progress with one of the major problems of contemporary astronomy.

We thank J.-U. Ness and A. Riffeser for fruitful discussions. R.S. acknowledges material and financial support from the Studienstiftung des Deutschen Volkes and Stiftung Maximilianeum.

REFERENCES

- Aumer M., Binney J., 2008, in preparation
 Benjamin R.A., Danly L., 1997, ApJ, 481, 764
 Bensby T., Feltzing S., Lundström I., Ilyin I., 2005, A&A, 433, 185
 Binney J., Dehnen W., Bertelli G., 2000, MNRAS, 318, 658
 Binney J., Lacey C., 1988, MNRAS, 230, 597
 Binney J., Tremaine, S., 2008, *Galactic Dynamics*, 2nd ed., (Princeton: PUP)
 Bland-Hawthorn J., Cohen M., 2003, ApJ, 582, 246
 Cescutti G., Matteucci F., François P., Chiappini C., 2007, A&A, 462, 943
 Cassisi, S.; Pietrinferni, A.; Salaris, M.; Castelli, F.; Cordier, D.; Castellani, M.
 Chiappini C., Matteucci F., Gratton R., 1997, ApJ, 477, 765
 Chiappini C., Matteucci F., Romano D., 2001, ApJ, 554, 1044
 Chieffi A., Limongi M., 2004, ApJ, 608, 405
 Colavitti E., Matteucci F., Murante G., 2008, arXiv:0802.1847
 Daflon S., Cunha K., ApJ, 617, 1115
 Dehnen W., 1999, AJ, 118, 1201
 Dehnen, W. & Binney, J., 1998, MNRAS, 298, 387
 de Jong R.S., 1996, A&A, 313, 377
 Edvardsson B., Andersen J., Gustafsson B., Lambert DL., Nissen P.E., Tomkin J., 1993, A&A, 275 101
 Flynn, C., Holmberg, J., Portinari, L., Fuchs, B., & Jahreiss, H. 2006, MNRAS, 372 1149
 Förster F., Wolf C., Podsiadlowski Ph., Han Z., 2006, MNRAS, 368, 1893
 François P., Matteucci F., Cayrel R., Spite M., Spite F., Chiappini C., 2004, A&A, 421, 613
 Fraternali F., Binney J., 2008, MNRAS, 386, 935
 Fukugita M., Peebles P.J.E., Hogan C.J., 1998, ApJ, 503, 518
 Gerssen J., Kuijken K., Merrifield M.R., 1997, MNRAS, 288, 618
 Grevesse N., Asplund M., Sauval A.J., 2007, S.S.Rv., 130, 105

Haywood M., 2006, MNRAS, 371, 1760
 Haywood M., 2008, MNRAS, 388, 1175
 Holmberg J., Nordström B., Andersen J., 2007, arXiv:0707.1891v1
 Ivezić Z., et al., 2008, arXiv:0804.3850v2
 Iwamoto K., Brachwitz F., Nomoto K., Kishimoto N., Umeda H., Hix W., Thielemann F.-K., 1999, ApJS, 125, 439
 Juric, M., Ivezić, Z., Brooks, A., et al., 2008, ApJ, 673, 864
 Just A., Jahreiss H., 2007, arXiv:0706.3850
 Kharchenko N.V., Piskunov A.E., Röser S., Schilbach E., Scholz R.-D., 2005, A&A, 438, 1163
 Kennicutt R.C., 1998, ApJ, 498, 541
 Kregel M., van der Kruit P.C., 2005, MNRAS, 358, 481
 Lai D.K., Bolte M., Johnson J.A., Lucatello S., Heger A., Woosley S.E., 2008, arXiv:0804.1370
 Limongi M., Chieffi A., 2008, <http://orfeo.iasf-roma.inaf.it/>
 Loktin A.V., Beshenov G.V., 2003, Astronomy Reports, 47, 6
 Maeder, A., 1992, A&A, 264, 105
 Marigo, P., 2001, A&A, 370, 194
 McMillan P. & Binney J., 2008, MNRAS, xx, xx (arXiv:0806.0319)
 Naab T., Ostriker J.P., 2006, MNRAS, 366, 899
 Nordström B., Mayor M., Andersen J., Holmberg J., Pont F., Jørgensen B.R., Olsen E.H., Udry S., Mowlavi N., 2004, A&A, 418, 989
 Oosterloo T., Fraternali F., Sancisi R., 2008, AJ, 134, 1019
 Pagel B.E.J., 1997, *Nucleosynthesis and Chemical Evolution of Galaxies* (Cambridge: CUP)
 Pettini M., Madau P., Bolte M., Prochaska J.X., Ellison S.L., Fan X., 2003, ApJ, 594, 695
 Pizagno J., Prada F., Weinberg D.H., Rix H.-W., Harbeck D., Grebel E.K., Bell E.F., Brinkmann J., Holtzman J., West A., 2005, ApJ, 633, 844
 Portinari, L., Chiosi, C., Bressan, A., 1998, A&A, 334, 505
 Reddy B.E., Lambert D.L., Allende Prieto C., 2006, MNRAS, 367, 1329
 Rich R.M., Howard C., Reitzel D.B., Zhao H.-S., de Propriis R., 2007, arXiv:0710.5162
 Robin, A.C., Reylé, C., Derrière, S. & Picaud, S., 2003, A&A, 409, 523
 Rocha-Pinto H.J., Maciel W.J., 1996, MNRAS, 279, 447
 Rolleston W.R.J., Smartt S.J., Dufton P.L., Ryans R.S.I., 2000, A&A, 363, 537
 Roman N.G., 1950, ApJ, 112, 554
 Roman N.G., 1954, AJ, 59, 307
 Roskar, R., Debattista, V.P., Stinson, G.S., Quinn, T.R., Kaufmann, T. & Wadsley, J., 2008, ApJ, 675, L65
 Samland M., Gerhard O.E., 2003, A&A, 399, 961
 Sancisi R., Fraternali F., Oosterloo T., van der Hulst T., 2008, A&ARv, 15, 189
 Schmidt M., 1963, ApJ, 137, 758
 Sellwood J.A. & Binney J., 2001, MNRAS, 336, 785
 Shaver P.A., McGee R.X., Newton L.M., Danlks A.C., Potasch S.R., 1983, MNRAS, 204, 53
 Shu F.H., 1969, ApJ, 158, 505
 Sommer-Larsen J., 1991, MNRAS 249, 368
 Thomas D., Greggio L., Bender R., 1998, MNRAS, 296, 119
 van der Kruit P.C. & de Grijs R., 1999, A&A, 352, 129

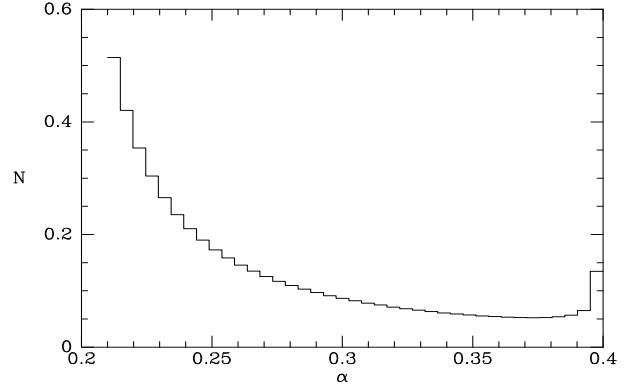


Figure 21. The distribution of α abundances predicted by equation (21).

van den Bergh S., 1962, AJ, 67, 486
 van der Kruit P.C., Searle L., 1982, A&A, 110, 79
 Venn K.A., Irwin M., Shetrone M.D., Tout C.A., Hill V., Tolstoy E., 2004, AJ, 128, 1177
 Vila-Costas M.B., Edmunds M.G., 1992, MNRAS, 259, 121
 Vilchez J.M., Esteban C., 1996, MNRAS, 280, 720
 Vorobyov E. I. & Theis Ch., MNRAS, 383, 817
 Z of Complex A
 Williams B.F., 2003, AJ, 126, 1312

APPENDIX: ORIGIN OF BIMODAL [O/Fe] DISTRIBUTIONS

We provide an analytic model of the development of the bimodal distributions of [O/Fe] evident in Fig. 9. We assume that star formation starts at $t = 0$ and that the SFR is $\propto e^{-Kt}$ for $t > 0$. Consistent with equation (5), we assume that a coeval group of stars formed at t' generates a rate of type Ia supernovae that vanishes for $t < t' + t_0$ and is subsequently $\propto e^{-k(t-t')}$. Then given that the rate of core-collapse SNe is proportional to the SFR, the rate of production of Fe is

$$\frac{dM_{\text{Fe}}}{dt} = \begin{cases} be^{-Kt} & \text{for } t < t_0 \\ be^{-Kt} + c \int_0^{t-t_0} dt' e^{-Kt'} e^{-k(t-t')} & \text{for } t \geq t_0, \end{cases} \quad (20)$$

where b and c are constants. Integrating this production rate, we obtain the iron mass at time $t > t_0$ as

$$M_{\text{Fe}}(t) = b \frac{1 - e^{-Kt}}{K} + \frac{c}{k - K} \left(e^{-(k-K)t_0} \frac{e^{-Kt_0} - e^{-Kt}}{K} - \frac{e^{-kt_0} - e^{-kt}}{k} \right). \quad (21)$$

In the approximation that SNIa do not contribute α elements, and that the delay in the production of these elements by a stellar population is $\ll 1/k$, the mass of α elements is $M_\alpha = (1 - e^{-Kt})a/K$ where a is a constant. Then equation (21) predicts that $\alpha \equiv M_\alpha/M_{\text{Fe}}$ equals a/b for $t \leq t_0$ and then drops rapidly towards its asymptotic value,

$$\alpha(\infty) = \frac{b}{K} + \frac{c}{Kk} e^{-kt_0}. \quad (22)$$

Fig. 21 plots the distribution at $t = 13$ Gyr of stars over α when the initial and asymptotic values of α are set to 0.4 and 0.2 and the other parameters are $K = 1/7$ Gyr, $k = 1/1.5$ Gyr and $t_0 = 0.3$ Gyr, which allows 0.15 Gyr for

white dwarfs to form and 0.15 Gyr for them to accrete prior to deflagrating.